REPORT DOCUMENTATION PAGE	Form Approved OMB NO. 0704-0188

1. REPORT DATE (DD-MM-YYYY) 17-02-2023	2. REPORT TYPE Thesis or Dissertation	3. DATES COVERED (From - To) -

4. TITLE AND SUBTITLE Vibrational properties of atomically thin semiconductors on ultra-flat metals	5a. CONTRACT NUMBER W911NF-19-1-0007
	5b. GRANT NUMBER
	5c. PROGRAM ELEMENT NUMBER 106012
6. AUTHORS Daniel C. Touzeau	5d. PROJECT NUMBER
	5e. TASK NUMBER
	5f. WORK UNIT NUMBER

7. PERFORMING ORGANIZATION NAMES AND ADDRESSES San Francisco State University 1600 Holloway Ave ADM 471 San Francisco, CA 94132 -1722	8. PERFORMING ORGANIZATION REPORT NUMBER
9. SPONSORING/MONITORING AGENCY NAME(S) AND ADDRESS (ES) U.S. Army Research Office P.O. Box 12211 Research Triangle Park, NC 27709-2211	10. SPONSOR/MONITOR'S ACRONYM(S) ARO
	11. SPONSOR/MONITOR'S REPORT NUMBER(S) 72495-RT-REP.19

12. DISTRIBUTION AVAILIBILITY STATEMENT

2 Approved for public release; distribution is unlimited

13. SUPPLEMENTARY NOTES

The views, opinions and/or findings contained in this report are those of the author(s) and should not contrued as an official Department of the Army position, policy or decision, unless so designated by other documentation.

14. ABSTRACT

15. SUBJECT TERMS

16. SECURITY CLASSIFICATION OF:			17. LIMITATION OF ABSTRACT	15. NUMBER OF PAGES	19a. NAME OF RESPONSIBLE PERSON
a. REPORT	b. ABSTRACT	c. THIS PAGE			AKM Newaz
UU	UU	UU	UU		19b. TELEPHONE NUMBER 415-338-2944

REPORT DOCUMENTATION PAGE (SF298)
(Continuation Sheet)

Continuation for Block 13

Proposal/Report Number: 72495.19-RT-REP

Report Title: Vibrational properties of atomically thin semiconductors on ultra-flat metals
Report Type: Ph.D. Dissertation

Publication Type: Thesis or Dissertation
Institution: San Francisco State University
Date Received: 17-Feb-2023 Completion Date: 12/20/22 7:20PM
Title: Vibrational properties of atomically thin semiconductors on ultra-flat metals
Authors: Daniel C. Touzeau
Acknowledged Federal Support: **Y**

Vibrational properties of atomically thin semiconductors on ultra-flat metals

Daniel C. Touzeau

October 2021

A thesis presented to the faculty of
San Francisco State University
In partial fulfilment of
The Requirements for
The Degree
Master of Science in Physics
by

Daniel C. Touzeau

San Francisco, California

December 2021

CERTIFICATION OF APPROVAL

I certify that I have read *Vibrational properties of atomically thin semiconductors on ultra-flat metals* by Daniel C. Touzeau and that in my opinion this work meets the criteria for approving a thesis submitted in partial fulfillment of the requirements for the degree: Master of Science in Physics at San Francisco State University.

Your adviser
Associate Professor of

Your committee member
Assistant Professor of

Your committee member
Professor of

Vibrational properties of atomically thin semiconductors on ultra-flat metals

Daniel C. Touzeau
San Francisco State University
2021

Transition metal Dichalcogenides, or TMDs are a class of semiconducting two dimensional materials with numerous possible applications in various fields such as biotechnology and optoelectronics. Molybendum disulfide or MoS_2 is the most widely used and studied TMD due to its ease of attainment and exfoliation. In this work, the effects of different substrates on the vibrational properties of MoS_2 were studied via Raman Spectroscopy. The substrates that were studied were Silicon dioxide (SiO_2), hexagonal boron nitride (h-BN), and atomically flat gold (Au). These measurements were carried out for temperatures ranging from 300k to 1.5k, for external magnetic field strengths ranging from 0 to 9 (and -9) Tesla, and for mono, bi, tri, and quadlayer MoS_2 samples. For each of the variables, shift in peak position, shifts in peak width, and changes in peak intensity were recorded and plotted. For the data on peak positions vs temperature, the data was fitted using a least squares linear fit and the rates of change of Raman peak energy with respect to temperature (α values) were found. This research found that peaks were generally (with one exception) redshifted on Au compared to SiO_2. As temperature went up, peaks redshifted as well. The B field dependence of the peaks was found to be negligible. The α values for the E' and A1' peaks on bilayer MoS_2/Au were found to be -0.0135 +/- 0.0035 cm^{-1}/K and 0.0143 +/- 0.0052 cm^{-1}/K, respectively. The α values for the E' and A1' peaks on trilayer MoS_2/Au were found to be -0.0086 +/- 0.0027 cm^{-1}/K and -0.0115 +/- 0.0033 cm^{-1}/K respectively.

I certify that the Abstract is a correct representation of the content of this thesis.

Chair, Thesis Committee Date

ACKNOWLEDGMENTS

First, I have to say I'm tremendously grateful to Dr. AKM Newaz, for taking the time to teach me, being astoundingly patient, and taking a chance on me when no one else would. Without him, there is not a doubt in my mind that I wouldn't be half the physics student I am today. Additionally, I must thank all of my fellow researchers that I have had the immense pleasure of meeting this past year: Bryce Baker for showing me the ropes not just experimentally but computationally as well. Vivianne Costa for basically being a second professor to me and for always taking the time to help me learn. To Shirin Jamali and Garrett Benson, who both, each in their own way, helped me along my path that led me to where I am today. I would also like to thank all of the physics faculty at SFSU, from Dr. Barranco all the way down to Caroline Alcantara and everyone in between, without whom none of my current accomplishments would be possible. I'd like to thank our collaborators at UC Berkeley for so graciously letting us use their Raman system. Our lab would also like to acknowledge our support from the Department of Defense Award (ID: 72495RTREP). Lastly, I have to thank my parents, my nuclear, and my extended family; all I have to say is: Look at me now!

Table of Contents

Contents

List of Tables

List of Figures

1 Background

1.1 Two Dimensional Materials

Ever since Konstantin Novosolev & Andre Geim isolated graphene via the method of mechanical exfoliation (exfoliation via 'Scotch' tape) the world of Two Dimensional materials has exploded in popularity and has been a hotbed for discovery and innovation [1]. Graphene is an allotrope of graphite (the same substance pencil lead and dry lubricant is made out of) meaning it is still made out of carbon, but in a single layer 1 atom thick i.e., a 2 dimensional material. Although Novosolev's and Geim's method was at first only used on graphene, it was soon expanded to encompass a wide range of 2-D materials from insulators to conductors and semiconductors. This explosion in the field was fueled by the need for increasingly thin and flexible electronics, as well as the rise of optoelectronics. These materials also present a novel way to study phenomena such as spin-valley physics, surface effects, quasi-particles, and quantum-confinement [2]. 2-D materials fall into one of six families of materials: insulators, semiconductors, half-metals, semi-metals, metals, and superconductors.

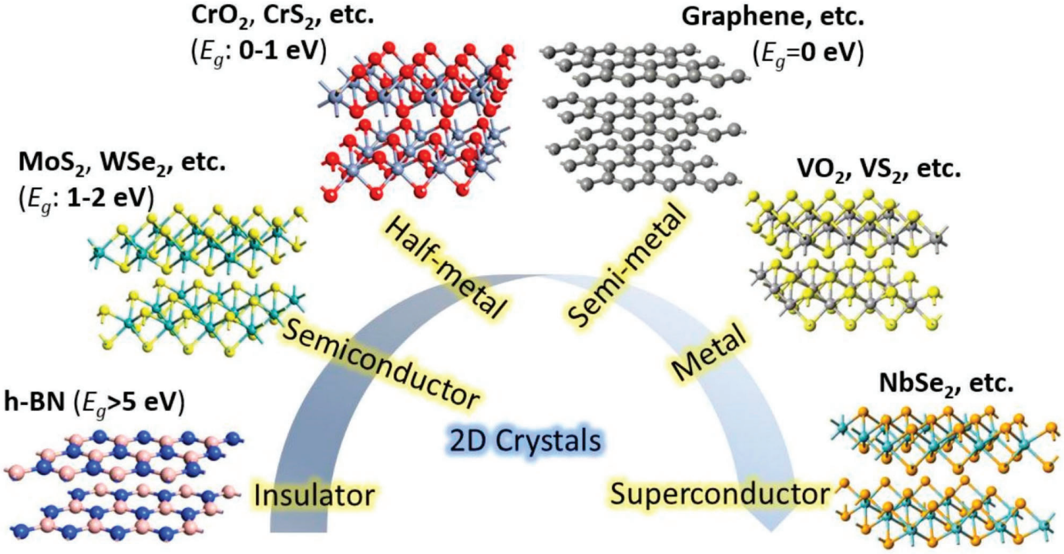

Figure 1.1: The families of 2-D materials. Arranged from least electrically conductive on the left, to most conductive on the right. Prominent examples from each family are provided next to their corresponding title. Underneath the names of the materials are their bandgaps in eV. Figure is reproduced from the paper Tanjil et al. [3]

2-D materials are placed in these groups by how well they conduct electricity, with insulators conducting almost no electricity, to conductors conducting the most electricity. With so many new materials being discovered, novel ways of constructing everything from transistors to pharmaceuticals were being discovered regularly as well. The most prominent advantage 2-D materials have is that they are, by definition, the thinnest materials known. This gives them an undeniable definite advantage when it comes to size, specifically in reducing the size of already existing technology. Not only this, but they also have the highest surface area to volume ratio of any class of materials, making them invaluable for biological applications such as drug delivery and bio-sensing. Originally as the field was emerging, researchers only had optical microscopy or transmission electron microscopy (TEM) to characterize these materials and verify their layer number. As the field has evolved however, techniques such as atomic force microscopy (AFM), 3D electron diffraction, scanning probe microscopy, and scanning tunneling microscopy were used to better verify and characterize materials.

1.2 Graphene

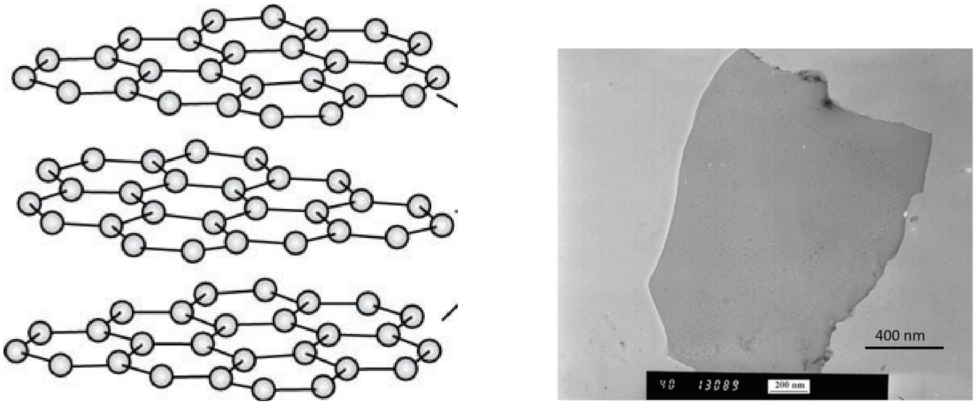

Figure 1.2: Left: Graphene monolayers stacked in graphite, as shown in a schematic cartoon. The grey circles represent carbon atoms. Right: Graphene flake as shown via optical microscopy. Scale bar provided at the bottom. Figures reproduced from Boysen et al. and Queens University [4] [5]

Graphene, originally observed via transmission electron microscopy (TEM) in 1962, at the time was not easily attainable in its monolayer form [6]. It wouldn't be until 2004 when Andre Geim and Konstantin Novosolev discovered that simply by pulling apart Scotch tape one was able to regularly yield single layers of graphene [1]. For this discovery, they were awarded the Nobel Prize in 2010. As for its physical properties, it resembles a dark gray to black powder or solid in its bulk form. However in its few layer to monolayer form, it is nearly transparent due to its thinness. It is remarkably durable as well, having a tensile strength of 130 GPa and has a Young's modulus of 1 TPa [7]. For comparison, that is 100 times stronger than steel at the same thickness. It is stable up to 400°C and is an excellent conductor of both heat and electricity, due mostly to its molecular structure. Its crystal structure is a plane of repeating hexagons in which each carbon is either single or double bonded to its neighbors as seen above in figure 1.2. Since it is an excellent conductor and so easily exfoliated, it has a plethora of applications and is used almost ubiquitously in devices with other 2-D materials. One possible drawback of graphene however, is that it has no bandgap: its valence bands and conduction bands touch, allowing charge carriers to go freely from one band to the next. This can be advantageous for some applications, but for applications requiring a 2-D semiconductor, new materials are needed.

1.3 TMDs

One family of promising 2-D materials are the transition metal dichalcogenides (TMDs), materials that are an element from periods 3 through 12 bonded to an element from period 16. Typically, in their bulk form they are light gray to dark gray metallic solids. All can be found in nature as various minerals such as molybdenite or drysdallite although some of these minerals can be extremely rare.

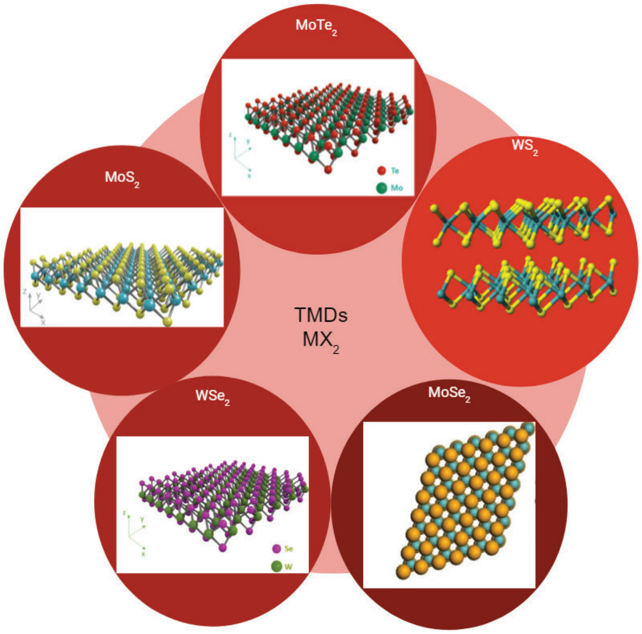

Figure 1.3: The family of TMDs. All TMDs generally have the same structure, a row of transition metal atoms situated between two layers of chalcogen atoms. All are easily mechanically exfoliable and all are semiconductors with direct bandgaps at the monolayer. They differ when it comes to the size of the bandgap and physical thickness of each layer. Figures reproduced from Eftekhari and Ossila [8]

The other popular method of attaining TMDs is through chemical vapor deposition (CVD), where the constituent atoms are exposed to a substrate in a reaction chamber under various conditions and allowed to react or decompose on the substrate [9]. Generally, the formula for TMDs can be written as MX_2 where M is the transition metal and X is the chalcogen. The most common among these are MoS_2, WS_2, $MoTe_2$, $MoSe_2$, WTe_2, and WSe_2. For all of these materials, the layer structure consists of a row of transition metal atoms in between 2 rows of chalcogen atoms. The unit cells for TMDs usually exhibit trigonal prismatic geometry, with the transition metal atoms serving as the coordination center [10]. Other geometries, such as octahedral or rhombohedral, have been found but are far less common. Each unit cell repeats to form a bi-hexagonal lattice, meaning if one looked from the top down onto one of the layers, one would see a hexagonal tiling much like graphene except that the layer is made of 3 rows of atoms and not one. Unlike other 2-D materials, all TMDs are semiconductors, with bandgaps ranging from 2.05 eV (WS_2) to 1.1 eV ($MoTe_2$). This makes them ideal candidates for use in van der Waals heterostructures, devices consisting of multiple 2-D materials stacked on top of each other, which are in turn stacked on or sandwiched between electrodes. These devices have the potential to be used in a variety of applications such as sustainability and green energy to reducing the dimensions of already existing technology. TMDs also exhibit unique spin-orbit splitting in monolayers due to strong spin orbit coupling, providing researchers new ways of studying spin-valley physics and spintronics [2]. TMDs are vital for scenarios where a 2-D material with a low (but not zero) bandgap is needed.

1.4 Molybdenum Disulfide

Of particular interest among TMDs is Molybdenum Disulfide (MoS_2) for its unique semiconducting and electromagnetic properties in its monolayer, bilayer, and multilayer forms as well as its relative ease in manipulation. This ease of manipulation arises due to the weak interlayer interactions caused by weak van der Waals forces between the layers. Since there is no out of plane bonding between S atoms of different layers, this leaves on the van der Waals forces to hold the layers together.

Figure 1.4: MoS_2 in its bulk form. From this flake, multiple samples can be mechanically exfoliated. This piece and every piece like it are made up of millions of individual layers of variable size. Figure reproduced from Spi supplies [11]

In its bulk form, it is a dark gray reflective solid off of which flakes can be peeled. It is found in nature as the mineral molybdenite, and is one of the more common TMD containing minerals. In its monolayer, bilayer, and multilayer form, it is a translucent blue solid, with the monolayer being the most transparent with the opacity increasing as layer number increases. In the monolayer form, MoS_2 has hexagonal or 2H symmetry as well as rhombohedral or 3R symmetry. In the bulk form, these monolayers are stacked on top of each other. For this research, only 2H MoS_2 will be discussed. In this structure, each Molybendum atom is covalently bonded to 6 Sulfide ions, with the Molybendum atom being the center for the 2H symmetry.

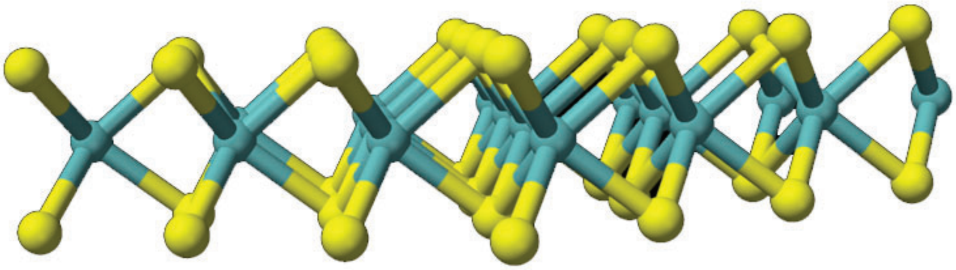

Figure 1.5: Cross section of monolayer MoS_2. Every monolayer is made up of a row of sulfurs on bottom and on top while the molybendum atoms are in between. The molybendum atoms are shown in light blue while the sulfur atoms are shown in yellow. Notice, how the Mo is slightly offset from the S, leading to the 2H bihexagonal geometry. Figure reproduced from Graphene Supermarket [12].

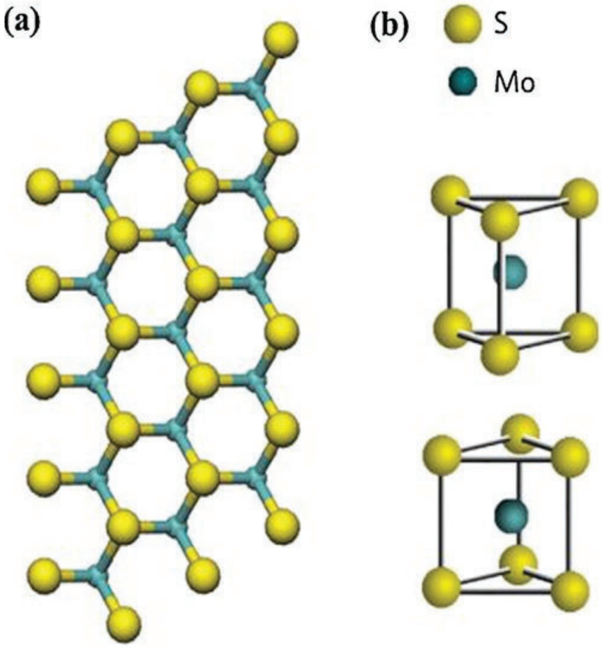

Figure 1.6: (a): Top down view of monolayer MoS_2. Note how the hexagonal pattern is nearly the same as for graphene and h-BN. (b): Unit cell structure of 2H and 1T MoS_2. In either configuration each molybendum is bonded to 6 Sulfurs, with the molybendum acting as the coordination center. Figure reproduced from Wu et al. [13]

1.5 Optical Properties

TMDs have two distinct regions in their electronic structure, known as bands, where charge carriers are allowed to exist. Charge carriers can be electrons or holes; when an electron gains the required energy to be promoted to the conduction band it leaves behind a hole in the valence band and this hole acts like a particle in its own right. Holes are positively charged and act as charge carriers in the material much like electrons. The highest allowed molecular orbital that electrons can exist in and still be bound to the molecule is called the valence band and the lowest range of vacant electron states is called the conduction band. The gap between the valence band maximum and the conduction band minimum is called the bandgap. It is also possible that holes and electrons can form a bound state, known an exciton, where the Coulomb forces between the electron and the hole bind the two together. These bound states can act like particles as well, transporting energy throughout the lattice and interacting with other charge carriers. This excitonic bound state is said to be hydrogenic in that it is similar to a hydrogen atom except when it comes to binding energy and size, with the binding energy of the exciton being much less than that of hydrogen and the size of an exciton being much larger than hydrogen. The hole and electron in an exciton can either have parallel or anti-parallel spins. In 2-D semiconductors, the binding energies and radii of excitons are enhanced due to quantum confinement. In such systems the excitons are confined to the direction parallel to the plane the semiconductor is on.

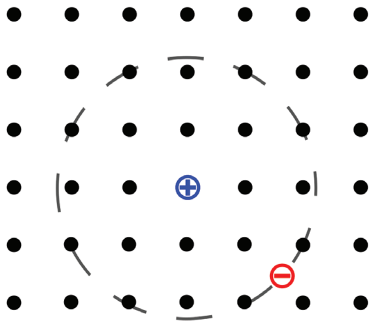

Figure 1.7: A graphical depiction of an exciton, with the positively charged hole (blue) in the center bound via the Coulomb force with the negatively charged electron (red). The black dots represent the lattice in which both hole and electron exist. Figure is reproduced from AxelFoley [14]

The creation of excitons can be stimulated by light: if a photo-active semiconductor absorbs a photon of greater energy than its bandgap then an electron from the valence band excites to the conduction band, leaving behind a hole which then binds via the Coulomb force with the excited electron to form an exciton. In this scenario, where only a photon needs to be absorbed, the material is said to have a direct bandgap. This is possible because the conduction band minima and valence band maxima sit at the same momentum value. Excitons can also form in indirect bandgap materials, but the process requires a few extra steps. In materials with an indirect bandgap, the valence band maxima and conduction band minima reside at different momentum values, but the optical transition requires that momentum is conserved. So for the exciton to form, the process must also involve the emission or absorption of a phonon, where the phonon momentum equals the difference between the electron and hole momentum.

1.6 Band Structure

MoS_2 is a semiconductor in both its bulk and monolayer forms with the bandgap for the bulk being 1.23 eV while the bandgap for the monolayer is 2.5 eV [15]. The reason for this difference is due to the quantum confinement effect taking hold at thicknesses below 1.5 nm i.e. when MoS_2 is in its monolayer form. Further, the bulk form has an indirect bandgap while the monolayer form has a direct bandgap. In figure 1.8 below, one can see the band diagram for monolayer, bilayer, and bulk MoS_2, with energy on the Y axis and symmetry points on the X axis. The corner points are denoted by G, with the middle of a rectangular face denoted by M and the middle of an edge joining two rectangular faces denoted by K.

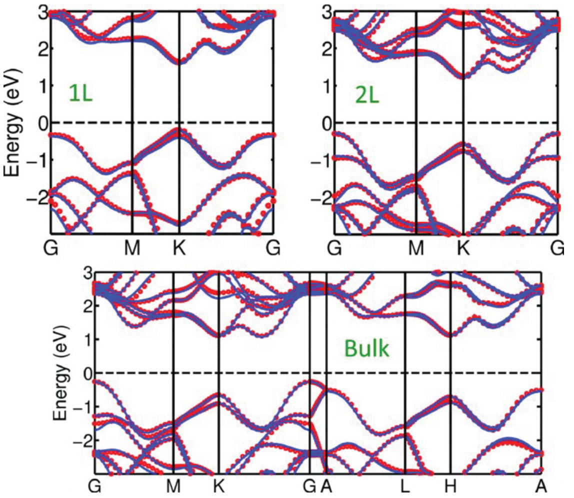

Figure 1.8: The band structure of 1 layer, 2 layer, and bulk MoS_2 as calculated by density functional theory (blue) and tight binding fitting (red). Energy in eV is shown on the Y axis while critical points are shown on the X axis. The Fermi level is denoted by the dotted line at 0 eV. One will notice that in the diagram for 1L, the band is closest to 0 at the K point, and at 2L it gets just a bit further away, until finally it's at its furthest in the bulk. Zahid et al. [16]

In the diagram for the bulk, L denotes the middle of an edge joining a hexagonal and rectangular face and A denotes the middle of a hexagonal face (M, K, and G denote the same things in the bulk as they do in the monolayer and bilayer). The majority of the conduction and valence bands are made up of the MoS_2 d orbitals, with direct energy gaps at K points of the Brillouin zone in the monolayer. MoS_2's uniqueness positions it as one of the prime candidates in the world of applications, such as spintronics, quantum computing, and optoelectronics to name a few. Further, since graphene has a bandgap of 0 eV, this puts MoS_2 at a definite advantage when it comes to those applications that require low current leakage and high sensitivity. In the band diagram of 1L, 2L, and bulk MoS_2 seen above in Figure 1.8, one can see the valence bands at the bottom of the figures below the Fermi level while the conduction bands are above the Fermi level, the Fermi level being denoted by the dashed line. Note that even though the bulk form has a closer bandgap at the G point, this gap is indirect, making the gap at the K point in the monolayer the most efficient at least when it comes to optical applications. In bilayer or multilayer MoS_2, since the band gap is indirect, the MoS_2 would have to absorb a phonon as well as a photon in order to promote its valence electron to the conduction band. However, due to lack of inversion symmetry in monolayer MoS_2, electron transitions take place only at the K point, thus turning it into a direct gap material. This lack of inversion symmetry has led to numerous inquiries into the spin-valley physics at play in monolayer MoS_2. MoS_2 has also exhibited some dependence on external magnetic field intensity [17]. In bulk materials, magnetism depends on spins being aligned on a macroscopic scale. For 2-D materials however, since spins only have to be aligned in 2 dimensions instead of 3, magnetism becomes much easier to induce. MoS_2 has exhibited diamagnetic as well as ferromagnetic properties at low temperatures [17]. As such, by performing Raman spectroscopy in the presence of an external magnetic field, one can use the corresponding changes in MoS_2's vibrational modes to study these magnetic properties.

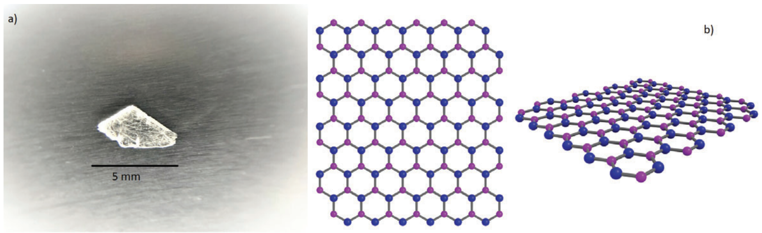

Figure 1.9: a): h-BN in its bulk crystal form. b): Layer structure of h-BN from the top down and isometric views. The boron atoms pictured in pink with the nitrogen atoms pictured in blue. Figure reproduced by 2D Semiconductors and Ossila [18] [19]

1.7 Hexagonal Boron Nitride

Hexagonal Boron Nitride or h-BN is a 2-D material like graphene and MoS_2. It exhibits hexagonal in plane geometry like graphene and MoS_2 except h-BN is an insulator whereas the other two are a conductor and semiconductor, respectively. In its bulk form, it looks like a fine white powder, in its multilayer form its flakes are deep blue to light blue, with the monolayers being nearly transparent. Like graphene and MoS_2, the atoms within the layer are strongly covalently bonded whereas the layers themselves are only held together by van der Waals forces, allowing flakes to be mechanically exfoliated in the same manner as graphene or MoS_2. Its crystal structure is similar to MoS_2 except all the atoms are in one plane instead of 2 to 3, leading to h-BN being much thinner than MoS_2. Other than its large bandgap and electrical resistivity, its also notable for its high dielectric constant and superior stability at high temperatures. All of these factors work in tandem to make h-BN one of the most used 2-D materials in the field.

2 Raman Scattering

2.1 Raman Scattering

Raman scattering is an inelastic scattering process, which means that unlike in other types of scattering the incident light in Raman spectroscopy does not have the same energy going out as it did coming in. Originally discovered in 1928 by C.V. Raman and his assistant K.S. Krishnan, their inquiry began with the question of why ocean water was blue [20]. It wouldn't be until 1930 that Raman was awarded the Nobel Prize for his seminal findings and contributions to the field. Raman scattering is a material absorbing a photon and exciting to a virtual energy state, it is called this because it is not an eigenstate. In fact, these virtual states cannot be observed at all, only their effects can be observed.

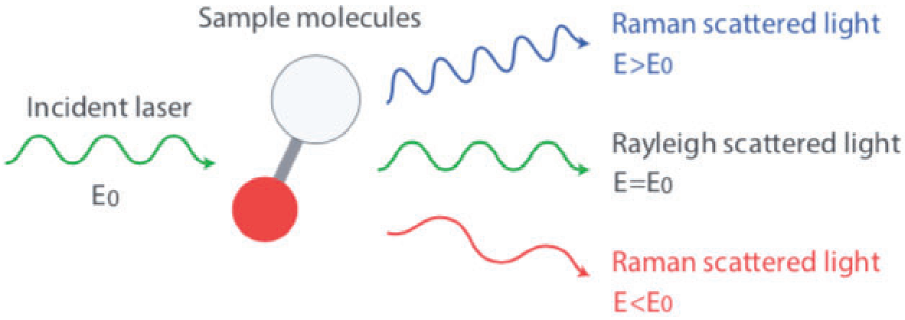

Figure 2.1: Raman scattering by a given molecule, drawn schematically. The incident laser has an energy of E_0 and once it interacts with the sample, it can take one of three paths. A fraction will be scattered at an energy greater than the incident wavelength (Anti-Stokes), at the same energy as the incident wavelength (Rayleigh), and at an energy less than the incident wavelength (Stokes). The Stokes and Anti-Stokes are the Raman scattering processes, and because of this, usually a notch filter is used to filter out the fraction of Rayleigh scattered light. Figure reproduced from Nanophoton [21]

Since the virtual state is not an eigenstate, it quickly decays back down to some lower vibrational energy state, releasing a photon of a specific wavelength in the process. Most of the light that is scattered back in this manner has the same energy as the incident light (Rayleigh scattering) but some photons have higher or lower energy once scattered. The photons with lower energy are said to be Stokes scattered and the photons with higher energy are said to be Anti-Stokes scattered. During Stokes scattering the material decays back down to a vibrational energy state above the ground state and during Anti-Stokes scattering the material starts from a higher vibrational energy state and ends up back at the ground state as seen in Figure 2.2. The reason for these shifts in energy is due to molecular vibrations that were happening in the material while the scattering was happening. Because energy is conserved, the incident light is then said to have excited that vibration, with the photon losing a portion of its energy in the process. These vibrations, called vibrational modes are distinct and are unique to every material, thus they provide a means of spectroscopic identification. These vibrations correspond to motions of the constituent atoms in the molecule, either along the bond length or in some direction around the center of mass of the molecule. These are contrasted with translational motion corresponding with the side to side motion of the whole molecule and rotational motion, corresponding with the rotation of the molecule about some axis.

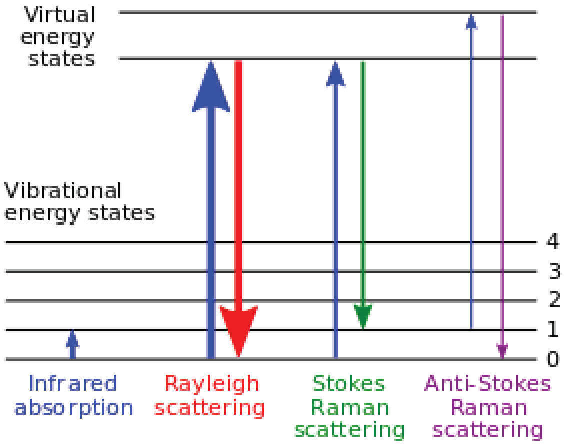

Figure 2.2: Graphical depiction of Rayleigh, Stokes, and Anti-Stokes scattering. The lines at the bottom represent vibrational energy states and are numbered 0-4 with o being the ground state. The lines at the top represent virtual energy states. Each of them are excited to some virtual energy state, with Rayleigh and Stokes scattering exciting to the same virtual state while Anti-Stokes excites to a higher virtual state. When each de-excites, Stokes scattering returns to a state above the ground state while Anti-stokes and Rayleigh Scattering return to the ground state. The Stokes and Anti-Stokes processes are the Raman processes. Figure reproduced from Pavlina2.0 [22]

2.2 Raman Spectroscopy

For Raman spectroscopy, only the Stokes and Anti-stokes modes are needed but not Rayleigh scattering, because the photons did not undergo a change in energy. Ordinarily, Raman spectroscopy is done with laser light due to the added benefit of knowing exactly the wavelength of light hitting the sample to simplify calculations later. Raman spectroscopy experimental setups usually consist of a laser, mirrors and/or fiber optics to redirect the laser, a dichroic mirror to split the beam, a microscope objective and stage, a notch filter, a line filter, and a spectrograph as seen in Figure 2.3. In the spectrograph, there is an entrance slit, a diffraction grating to split the light from the sample into its constituent wavelengths, a CCD to collect the light and turn it into data, and mirrors to reflect the light from one component to the next. All of the optical components and spectrograph are fastened to an optical table for stability and to align the beam path to the sample and detector. Various other components could be added for different purposes, such as polarizers, lenses, and lasers of different wavelengths. When Raman spectroscopy is performed, the laser starts by going through a line filter to mitigate the amount of power reaching the sample and detector. Then the laser gets reflected into a dichroic mirror that shoots one beam through the objective lens and onto the sample. The light from the sample then goes back through the dichroic mirror and through a notch filter to remove the Rayleigh scattered light. Then the beam enters the spectrograph through the entrance slit and is diffracted off of the diffraction grating, splitting the beam into its component wavelengths. These are then reflected off a mirror and into a CCD which finally sends this data to a computer to be analyzed. This setup and process is illustrated in Figure 2.3. However, Figure 2.3 depicts only the most basic Raman setup, usually there are other components such as a light path to a camera so that the sample can be imaged. Typically such a setup would include a camera and a separate light path that doesn't interfere with the beam path.

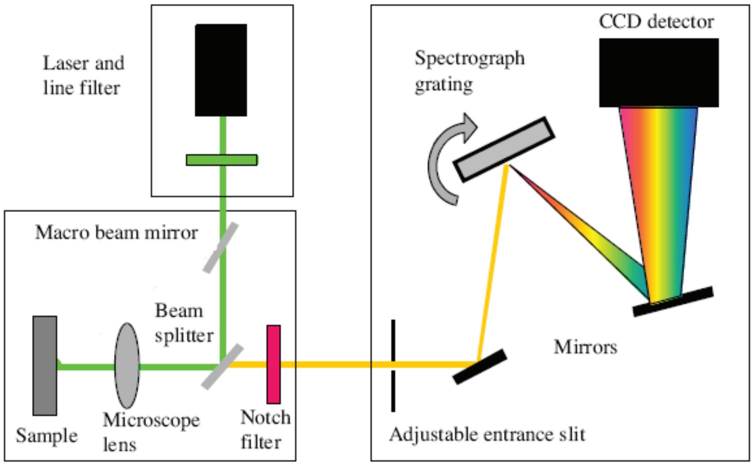

Figure 2.3: Diagram of a typical Raman spectroscopy setup. The beam starts from the laser and then encounters the line filter before going on to the macro beam mirror. Then it encounters the dichroic mirror and one beam goes to the microscope objective and then on to the sample. The scattered light coming off the sample then goes back through the dichroic mirror and into the spectrograph. Then, the beam goes through the entrance slit and then reflects off the diffraction grating that splits the light into its constituent wavelengths. These are then reflected into the CCD detector. Figure reproduced from SAS UPenn [23]

The difference between the scattered wavelength and the incident wavelength is known as Raman shift (δ) given by the equation

$$\delta\ cm^{-1} = \frac{10^7}{\lambda_{ex}\ nm} - \frac{10^7}{\lambda\ nm}$$

The spectrum attained contains peaks corresponding to the vibrational modes of the material. The data is plotted on a graph with photon intensity on its Y axis in arbitrary units and Raman shift in cm^{-1} on the X axis. Each one of these vibrational modes are caused by phonons of a different energy and frequency. Phonons are the quanta of vibration in condensed matter. Phonons are known as a quasi-particle meaning they behave like particles (have spin, can be absorbed and released, etc) but are not particles in the classical sense. Keeping with the classical analogy, phonons would correspond to the normal modes of a classical spring and mass system. In Raman spectroscopy, the frequency of a phonon is equal to the difference between the incident photon frequency and the scattered photon frequency. This frequency can be measured via Raman spectroscopy, and this is what makes Raman spectroscopy so useful in determining the vibrational structure of the material. When categorizing all the different motions a given molecule could undergo, it is useful to use the irreducible representation given by

$$\Gamma = \Gamma_{trans} + \Gamma_{rot} + \Gamma_{vib}$$

which describes every possible rotation, translation, or vibration that leaves the molecule unchanged. Typically, rotation only comes into play when gasses are involved, so this term is usually discarded. In the field of 2-D materials, translational terms can also be discarded since these terms do not hold information about the vibrational structure of the material. This leaves only the vibrational terms, which are determined by the degrees of freedom available to the lattice. For MoS_2 the irreducible representation is [24] :

$$\Gamma_{vib} = A_{1g} + 2A_{2u} + 2B_{2g} + B_{1u} + E_{1g} + 2E_{1u} + 2E_{2g} + E_{2u}$$

Each of the above terms corresponds to a unique vibration that leaves the MoS_2 unchanged [24]. Only 3 of these modes are Raman active, E_{1g}, A_{1g}, and E_{2g}. Each one of these peaks is caused by a phonon of a different frequency, and the Raman peak for E_{2g} occurs around 380 cm^{-1} and the peak for A_{1g} occurs around 400 cm^{-1} at room temperature [25]. It is also worth noting that unlike in the E_{2g} mode where the constituent atoms in the lattice move collectively from side to side within the layer, in the A_{1g} mode the sulfur atoms move closer and further apart while the molybendum atoms remain still, resulting in out-of-plane, interlayer motion of the sulfur atoms as seen in Figure 2.4. In the bilayer and bulk, the A_{1g} mode is dampened due to limited space in between layers for the sulfur atoms to move in. However, in the monolayer, there is unlimited space for the sulfurs to move in resulting in greater A_{1g} intensity. This knowledge provides a way to determine layer number via Raman spectroscopy. Additionally, it is possible to determine layer number via peak shift and changes in peak width.

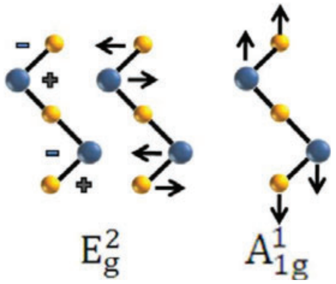

Figure 2.4: E_{2g} and A_{1g} Raman modes of MoS_2. Both of these modes are due to phonons in the crystal lattice. As with Figure 2, Mo is shown in blue while S is shown in yellow. Two layers are shown here with the solid black lines indicating covalent bonds. Notice how the E_{2g} mode stays in plane while the A_{1g} mode goes out of the plane. Figure reproduced from Yuan et al. [26]

3 Experimental Methods

3.1 Sample Fabrication

This section details all of the methods that went into fabricating samples, fabricating the atomically thin Au, and how some of the multilayer samples were made. For sample fabrication, a modified version of mechanical exfoliation was used. To start, a large piece of bulk MoS_2 was placed between two pieces of scotch tape and then slowly pulled apart. Then, blue polyvinyl chloride (PVC) tape was placed onto one of the pieces of tape and left to sit for 1-5 minutes. Afterwords, this blue electrical tape was pulled off of the Scotch tape and then a clean piece of Scotch tape was placed on the blue tape. The exfoliation continued in this manner until a color change in the sample indicating a monolayer could be seen. For the samples on SiO_2, the sample on Scotch tape was placed on a SiO_2 chip and then placed on a hotplate for 20-25 minutes at 50 °C. When the time had elapsed, the Scotch tape was peeled off slowly and the sample was stored in a 3x3 Si chip case.

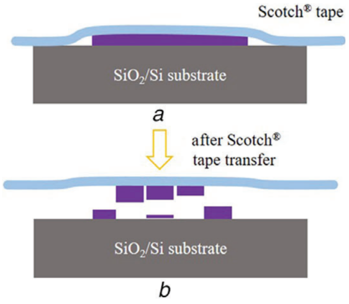

Figure 3.1: The process of mechanical exfoliation. a) The Scotch tape containing the material is pressed onto the SiO_2/Si substrate. b) The Scotch tape is peeled off leaving thin layers of material behind on the substrate. Figure reproduced from Budania et al. [27]

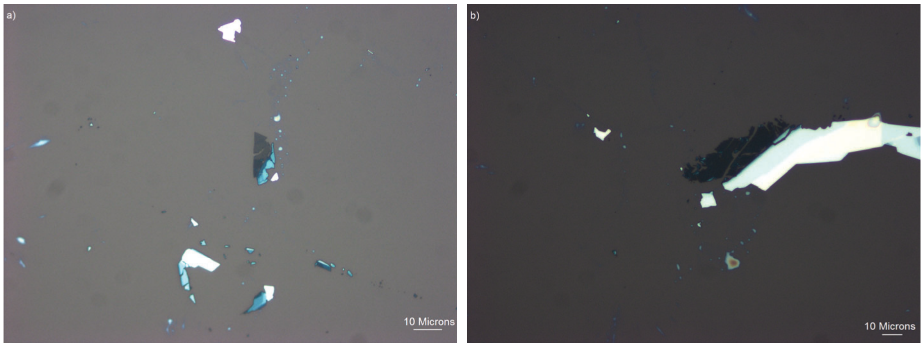

Figure 3.2: a) Monolayer MoS_2 connected to bi and trilayer MoS_2 which is in turn connected to a bulk piece on SiO_2. b) Bilayer MoS_2 connected to a larger bulk piece on SiO_2. Both pictures are at 50x magnification.

3.2 Atomically Thin Au Fabrication

For the samples on atomically thin gold, a wafer of prime-grade silicon was cleaned at 70°C for 10 minutes in a 4:1:1 mixture of water, ammonium hydroxide, and hydrogen peroxide. Then this wafer was rinsed with deionized water and dried under an argon atmosphere. Then, this wafer was placed in a bell jar at a pressure of 10^{-7} Torr while 150 nm of gold was thermally evaporated onto the wafer at 5 Å/s. This process produces gold coated Si wafers but thermal evaporation leaves the gold surface rough, at least in terms of 2-D materials. To create the atomically thin surface needed for the experiment first, a two part epoxy (Bisphenol A-epichlorohydrin polymer and 3-2,3-Epoxypropoxypropyltrimethoxysilane) was applied to 1cm x 1cm chips of SiO_2. Then, the Si wafer with the Au on it was cut into similarly sized pieces and placed face down onto the epoxy and silicon. Then the chips were pressed with $\sim$ 10 kgs and left to set for 12-24 hours. Afterword, the original piece of silicon and epoxy were removed, leaving behind atomically thin gold. The Scotch tape containing the sample was then applied to the atomically thin gold for 20-25 minutes and, after this time had elapsed, peeled off. To verify the layer number of the sample and to pinpoint its location on the chip optical microscopy at 5x, 10x, 20x, and 50x magnification was used. Once the sample had been identified, then the samples were characterized via Raman spectroscopy.

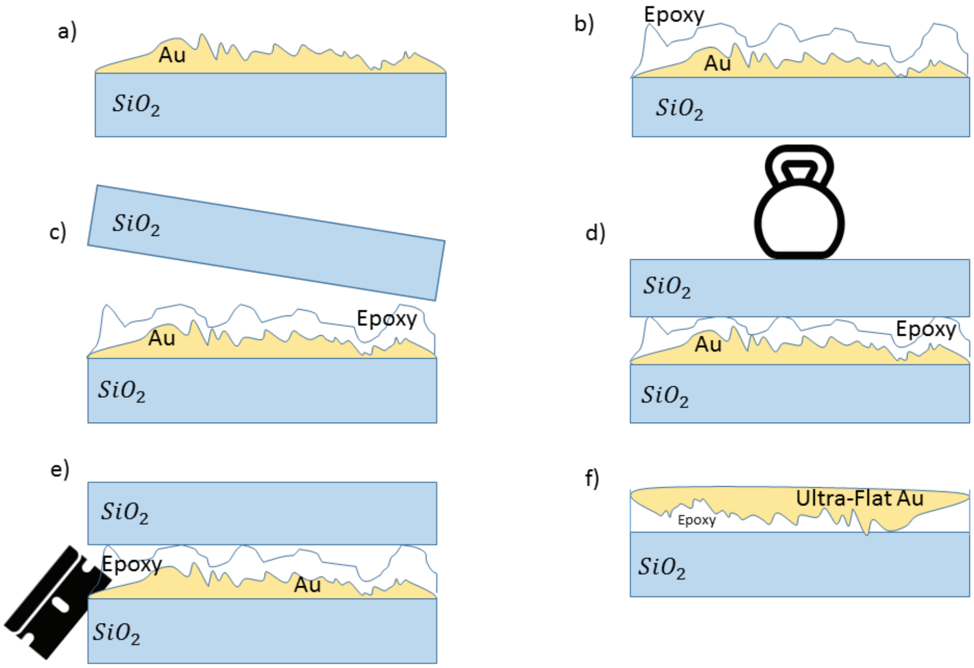

Figure 3.3: a) The native piece of SiO_2 with rough Au is selected. b) Epoxy is applied to the rough Au surface. c) A clean SiO_2 chip is applied to the epoxy. d) Approximately 10 kg is set on the stack for 12-24 hours. e) A razor is used to cleave the stack apart. f) The resulting atomically thin Au on epoxy and SiO_2.

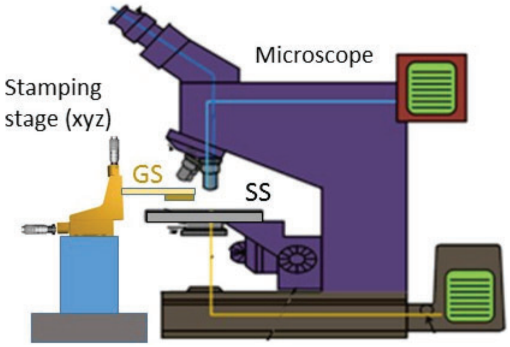

Figure 3.4: A schematic cartoon of the custom built transfer stage used to fabricate the samples and devices. The microscope is shown above in purple with the heated sample stage shown directly below. To the left, the stamping stage is shown in yellow with X/Y adjustment knobs attached at the top and on its left. Not shown above are the X/Y knobs for moving the stage. In sample fabrication, the sample on PET goes in the stamping stage and the sample on gold goes on the sample stage.

3.3 Transfer Stage

Pictured above in figure 3.4 is the custom made nano-fabrication stage used in the sample fabrication process. The stage consists of a microscope objective with course and fine adjustment knobs, atop of which sits a CCD connected to a nearby computer. Below the objective is the heated stage, which can be turned a full 360°to produce samples with an angle offset. Below the stage are the X and Y adjustment knobs to move the stage left, right, up, and down. To the left of the stage is the microcontroller, into which an aluminium slide containing the sample is placed. The microcontroller has X and Y adjustment knobs of its own and for fine adjustments, it can be controlled by the nearby computer. All of these components are fastened to an optical table that isolates them from vibrations that occur in the surrounding environment. The CCD is accessed on the computer by AmScope and the microcontroller is controlled on the same computer by ZaberConsole stage manipulation software. For preparing a sample for the transfer stage, one cuts a glass microscope slide into a 5 cm x 5 cm square. Then, a cut .5 cm x .5 cm piece of piece of Polyethylene terephthalate (PET) is placed onto the slide with a piece of double sided tape and this slide is fastened to the aluminum slide also with double sided tape. The aluminium slide is then inserted into the microcontroller where it is pressed onto a clean SiO_2 chip for $\sim$1 min to flatten the underside of the PET. During this process the temperature of the stage can be set to 60°C in preparation for the rest of the process. Next, the sample is placed on the stage at 60°C and the location of the monolayer, bilayer, or trilayer is found with the microscope attached to the stage. Next, the microcontroller is used to press the PET onto the sample to pick it up. After the first sample is on the PET, the chip is removed from the stage and a second chip containing another sample is placed on the stage. For samples with an offset, this is when one turns the stage to the desired angle. Finally, the layer on the PET is pressed onto the layer on the stage creating the bilayer. This newly made bilayer sample is then picked up with the PET and placed on a clean chip of SiO_2 and left to adhere at 140 °C for 20 to 30 minutes. Once this time had elapsed, the slide was lifted off, leaving the chip with melted PET on it. To remove this PET, the chip was submerged in a bath of dichloromethane (DCM) at 75°C for 45 minutes. When the PET had been removed, optical microscopy was used to confirm the sample's presence on the chip.

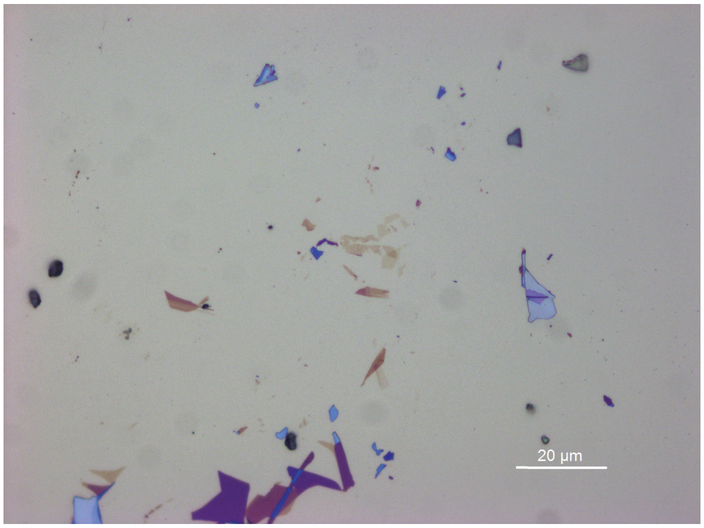

Figure 3.5: Image of bilayer MoS_2 sample made with transfer stage. Magnification is 50x.

3.4 Transfer on atomically thin Au

Due to the epoxy used in the fabrication of the atomically thin Au, samples on Au could not be heated or submerged in DCM or else the epoxy would deform making the Au not atomically thin or the Au would wash away entirely. Thus, a modified procedure had to be used. First, Polydimethylsiloxane (PDMS) was cut into 1 cm x 1 cm piece and placed onto a cut 5 cm x 5 cm cut microscope slide. This slide was then adhered to the aluminium slide via double sided tape in the same manner as was used in the regular transfer process. The sample making process then proceeded much in the same manner as the process for SiO_2 except the stage was never heated so as to not deform the Au, and the flakes were picked up with the PDMS and not PET.

4 Raman Spectroscopy Setup

4.1 Raman Setup

For the temperature dependant Raman stage, the Attodry (2100, attoCFM, and atto3DR) closed cycle cryostat system was used in conjunction with a custom made optical setup as seen in Fig 4.1 and a confocal microscope objective of 100x magnification. In the optical setup, the beam started by going through a variable filter to mitigate the power reaching the sample, the detector, and camera. Next, the light went into a fiber optic cord that was connected to the optical table on top of the cryostat.

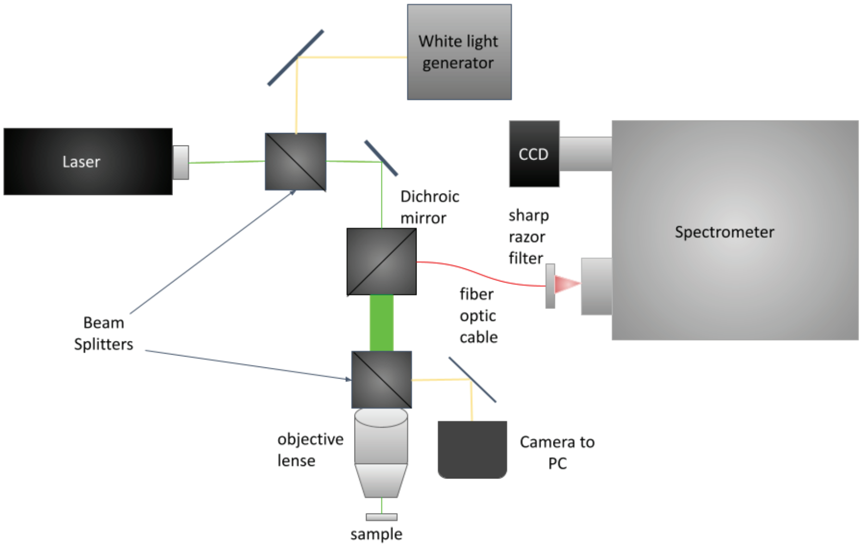

Figure 4.1: A schematic of the optical table used in conjunction with the Attodry system. The 532 nm laser is shot into a fiber optic which leads to the optical table where it bounces off of a mirror before going into the dichroic mirror. One beam goes into the objective and then down to the sample. Then, the signal from the sample goes through a sharp razor filter and is then guided by a multi-mode optical fiber into the spectrometer. Finally, the light gets bounced into the CCD where it is then converted into data.

Then, the beam is reflected by a dichroic mirror and then travels down into the cryostat. The signal from the sample then goes back through a sharp razor filter and is collected into a multi-mode fiber optic cable that guides the light into the spectrometer. The signal then enters the spectrometer where it is dispersed into its component wavelengths, which then fall into the charge coupled device (CCD). The CCD camera is coupled to a nearby computer which records the spectrum. The laser, spectrometer and sharp razor filter are on their own vibration-free optical table and the rest of the optical setup is on a movable optical board mounted on top of the crysostat. We use a diode pump laser of wavelength 532 nm and power of 50 mW. The spectrometer used in the data acquisition is an Andor Shamrock 303i system with a 500mm focal length and an f number of F/6.5. The gratings that are used are 300 l/mm, 1200 l/mm, and 1800 l/mm gratings with the resolution at 1200 l/mm being 0.07 nm. Used in conjunction with the spectrometer was a thermoelectrically cooled iDus CCD with a sharp razor filter at the aperture to filter out Rayliegh scattered light. The samples on both Au and SiO_2 are placed on the attodry stage along with a SiO_2 chip containing quantum dots for calibration and then these are lowered down into the body of the attodry 2100. For alignment of the system, the laser is aimed at the quantum dot and set to the 300 l/mm grating while the spectrometer acquires continuously. For regular acquisitions, the program used with the spectrometer (Andor Solis) displays the data after the acquisition is done. For continuous acquisitions, the data is displayed in real time. The data is displayed on a graph of intensity (counts on the CCD) vs Raman shift (cm^{-1}). During alignment, the beam path is adjusted and modified such that the counts on the CCD are maximized. For calibration, the laser is taken off of the quantum dots and aimed at pure SiO_2 where a 3 minute acquisition is taken and then 3 more acquisitions are taken. This data is then used not only to make sure that the Raman shift range (X axis in Andor) was correct, but also to aid the program used in data analysis. Both of these processes had to be done remotely with separate software to move the stage (Daisy) and view the stage (AmScope camera software) due to the cryostat being in a cryogenic environment. Additionally, the only eyepiece on the stage is at a magnification of 100x. For cryogenic Raman system calibrations on h-BN and Au, the calibration proceeded in the same way, except the laser took acquisitions on pure Au and h-BN instead of SiO_2. To compare our Raman measurement with a commercially built Raman system, we gathered room temperature Raman spectroscopy data using a Renishaw Invia Raman system available at UC Berkeley. The Raman system was used in collaboration with Prof. Junqiao Wu's group in the Material Science Department. Their equipment uses a 488 nm laser and 50x microscope objective of $\sim$0.85 numerical aperture.

4.2 Raman Spectroscopy Measurement

The Raman measurements were conducted on mono, bi, and trilayer MoS_2 and the substrates used were h-BN, atomically thin Au, and SiO_2.

We measure Raman spectra at varying temperatures, layer numbers, and substrates. For temperature dependence measurements, Raman measurements were taken with the spectrometer set to the 1200 l/mm diffraction grating. For each acquisition, the laser was aimed at the sample and left to acquire for 5 minutes after which, two more acquisitions like these were taken. We measure the Raman spectrum from 1.5k to 100k in 10k intervals. After 100k, the Raman spectrum was recorded at every 50k increment until we reached 300k.

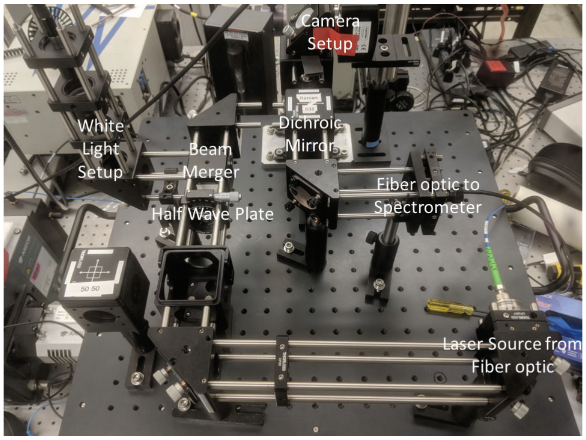

Figure 4.2: Top down view of the optical setup used for Raman data acquisition. The dichroic mirror and CCD setup are mounted above the aperture that leads down to the stage, while the white light path is on the left side after the polarizer. The black fiber optic cable leads to the spectrometer, while the blue fiber optic cable leads to the laser.

For external magnetic field dependence measurements, only monolayer and bilayer MoS_2 samples on atomically thin gold were studied. All magneto-Raman measurements were done at a temperature of 1.5 k only. The variables to be measured against change in B field were peak position, width, and intensity. The grating, exposure time, and number of acquisitions stayed at 1200 l/mm, 5 minutes, and 3 exposures each, respectively. However, when the three 5 minute acquisitions were done, the magnetic field was raised by 3 Tesla each time. The experiment continued in this manner until 9T was reached. After the positive B field measurements, negative B field measurements were taken in the same way starting from -3T. After three 5 minute acquisitions the magnetic field was lowered by 3T until -9T was reached.

4.3 Data Analysis

To analyze the Raman data taken from the MoS_2 samples, Origin 7 32-bit data analysis software was used to reduce, compare, and fit the data as well as to make the graphs of temperature vs peak position, temperature vs intensity, and temperature vs width. First, the raw data was taken from the text files written by Andor Solis and imported into Origin. Then, the raw data was plotted for the acquisitions for the monolayer, bilayer, trilayer, and bare substrate. Next, the three acquisitions for a given temperature were averaged, and the background from the substrate was subtracted. Next, a baseline was fitted to the data for the monolayer, bilayer, and trilayer Raman data for each substrate and subsequently subtracted.

Next, a double lorentzian of the form

$$y = [y_1 + \frac{2A}{\pi} \cdot \frac{w_1}{4(x_1 - x_c)^2 + w_1^2}] + [y_2 + \frac{2B}{\pi} \cdot \frac{w_2}{4(x_2 - x_d)^2 + w_2^2}]$$

(where y_1 and y_2 are the offsets, A and B are the areas, w_1 and w_2 are

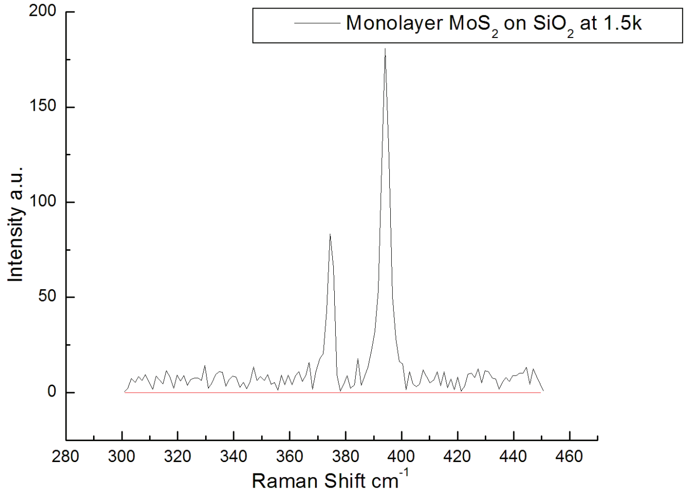

Figure 4.3: Baseline fitting of MoS$_2$ raw Raman data on SiO$_2$ at 1.5k. The red line at 0 intensity is the fitted baseline. This is only an intermediate step in the data reduction and fitting process. After this step, a double lorentzian will be fitted to the peaks and the area under each peak will be integrated to find intensity.

the widths, and x_c and x_d are the centers) was fitted to the E' and A_1 peaks for all data sets. This fit provided values for the peak positions as well as the width of the peaks. Then, the area under each of the peaks was integrated to yield the intensity of each peak. The analysis continued in this manner for the rest of the data at each of the temperatures and for each of the substrates for the monolayer as well as the bilayer and trilayer. Then, with all of the data compiled, graphs of temperature vs. peak position, temperature vs. intensity, and temperature vs. width were created and a least squares linear fit of the form

$$y_i = b_1 x_1 + b_0 + \epsilon$$

(where b_0 is the x-intercept, b_1 is the slope, y_i is the predicted value, x_1 is the data point, and ϵ is the error) was applied to the graphs of temperature vs. peak position to yield α values. An α value is the first order temperature coefficient for a given sample and is equal to $\frac{\partial\omega}{\partial T}$ and can be found by finding the slope on a graph of peak position vs. temperature for a given sample. Graphs of peak position vs temperature, width vs. temperature, and intensity vs. temperature were made for the magneto-Raman data as well. However, a linear fit was not applied to the graphs of peak position vs. temperature for the magneto-Raman data.

5 Results

5.1 Room Temperature Raman

In all of the Raman data (excluding 1L-MoS_2/Au), multiple peaks can be seen but only two are of interest. In the figures of Raman shift vs Intensity below, the two quite sharp peaks at lower wavenumber are the peaks of interest (A_1 and E') while (on atomically thin Au) the broad peak at higher wavenumber is due to a combination of the Si peak and the effects from the atomically thin Au. To the best of our knowledge, Raman spectroscopy studies of MoS_2 on SiO_2 and h-BN have been conducted but MoS_2 on atomically flat Au has not been studied.

5.1.1 MoS_2/SiO_2

For all room temperature Raman measurements of MoS_2/SiO_2, the 488 nm laser was set to a power of 80 μW. For the 1L, 2L, 3L, and 4L MoS_2/SiO_2 data at room temperature, we observe the A_1 peak occurring around 405 cm^{-1} and the E' peak occurring around 385 cm^{-1}. We observed that as layer number increased, intensity of both peaks increased. For 1L and 3L MoS_2, the A_1 peak was more intense than the E' peak, but for 2L and 4L MoS_2 the E' peak was more intense.

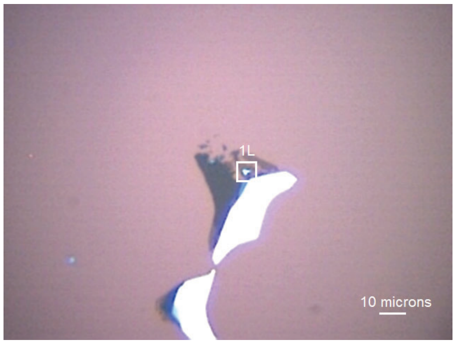

Figure 5.1: Picture of monolayer MoS_2 sample on SiO_2 at 50x magnification. The region the data was gathered from is marked with a white box.

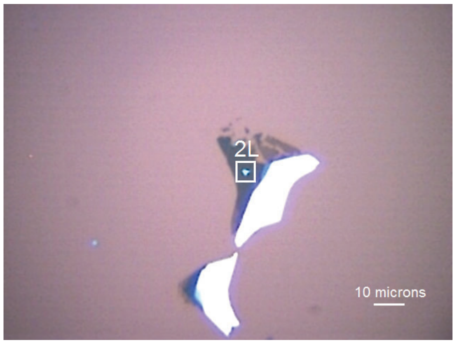

Figure 5.2: Picture of bilayer MoS_2 sample on SiO_2 at 50x magnification. The region the data was gathered from is marked with a white box.

There was a several orders of magnitude increase in intensity when going from 2L to 3L for both peaks. However, the intensity of both peaks increased only marginally when going from 1L to 2L and from 3L to 4L. We observed that as layer number increased, the widths of each peak did not change. For all layer numbers the A_1 peak was observed to be wider than the E' peak. These results are consistent with numerous other room temperature studies of MoS_2/SiO_2 [28]. These measurements act as a guide to confirm the system is accurate and also as a comparison to measurements on atomically flat Au.

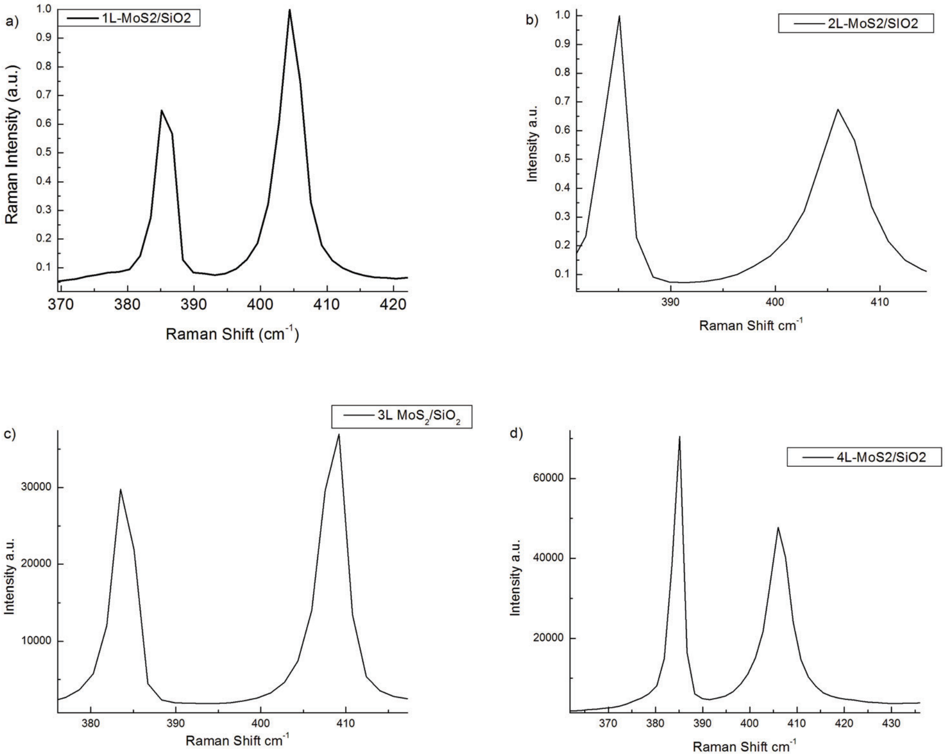

Figure 5.3: a)The temperature dependant Raman data from monolayer MoS_2 on SiO_2. b) The temperature dependant Raman data from bilayer MoS_2 on SiO_2. c) The temperature dependant Raman data from trilayer MoS_2 on SiO_2. d) The temperature dependant Raman data from quadlayer MoS_2 on SiO_2.

5.1.2 MoS_2/Au

For all room temperature Raman measurements of MoS_2/Au, the 488 nm laser was set to a power of 80 μW to be consistent with the measurements for

MoS_2/SiO_2. For the 1L MoS_2/Au measurements, we observed the E' peak and A_1 peak occurring around 375 cm^{-1} and around 400 cm^{-1} respectively. This is about a 10 cm^{-1} redshift for both peaks compared to SiO_2. Also, the A_1 peak is wider and less intense than it is on SiO_2. For 2L MoS_2/Au, the E' peak occurred around 380 cm^{-1} and the A_1 peak occurred around 405 cm^{-1}. This is about a 5 cm^{-1} redshift in the E' peak but not the A_1 peak. Also, the E' peak increased in width and dropped in intensity compared to SiO_2. For 3L and 4L MoS_2/Au, both peaks remained at 385 cm^{-1} for E' and 405 cm^{-1} for A_1, and there widths and intensities increased only slightly. The A_1 peak for 3L and 4L MoS_2/Au was wider than the E' peak just as it was for SiO_2. Also, worthy of note is how the distance between the peaks increased from 1L to 2L and from 2L to 3L. This inter-peak distance stopped increasing however from 3L to 4L.

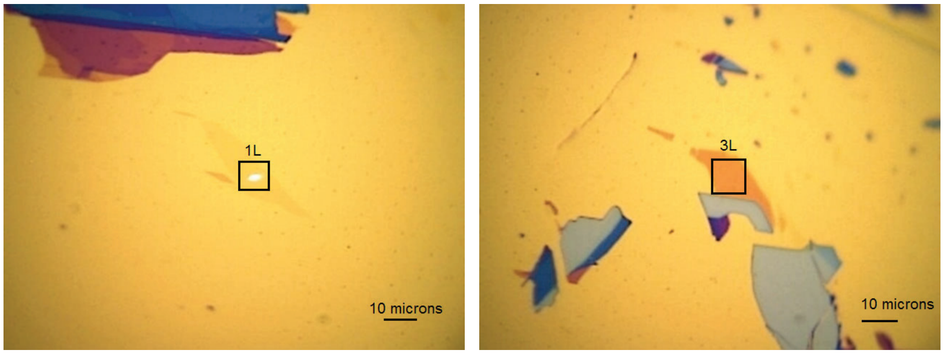

Figure 5.4: Left: Picture of monolayer MoS_2 sample on atomically thin Au at 50x magnification. The region the data was gathered from is marked with a black box. Right: Picture of trilayer MoS_2 sample on atomically thin Au at 50x magnification. The region the data was gathered from is marked with a black box.

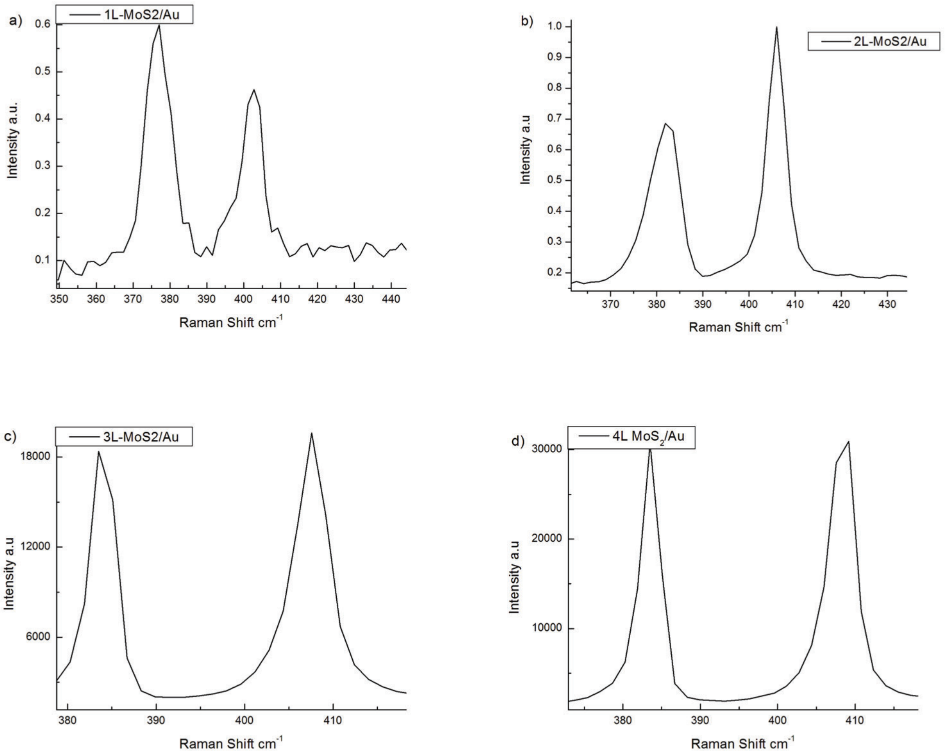

Figure 5.5: a) The temperature dependant Raman data from monolayer MoS_2 on atomically thin Au. b) The temperature dependant Raman data from bilayer MoS_2 on atomically thin Au. c) The temperature dependant Raman data from trilayer MoS_2 on atomically thin Au. d) The temperature dependant Raman data from quadlayer MoS_2 on atomically thin Au.

5.1.3 Comparison of Raman spectrum of MoS2/SiO2 with MoS2/Au

The Raman spectroscopy measurements of 1L, 2L, 3L, and 4L MoS_2 samples demonstrated that Raman peaks are shifted for samples on SiO_2 compared to the samples on atomically thin Au as seen below in figure 5.6. For the samples on Au, almost all peaks redshifted, except for the A_1 peak on quadlayer MoS_2, which are blueshifted when on Au. As for the change in intensities with respect to substrate, on mono, tri, and quadlayer MoS_2 the intensity of both peaks was greater on SiO_2 than it was on Au. The one exception being the A_1 peak for the bilayer MoS_2, which was more intense on Au than it was on SiO_2.

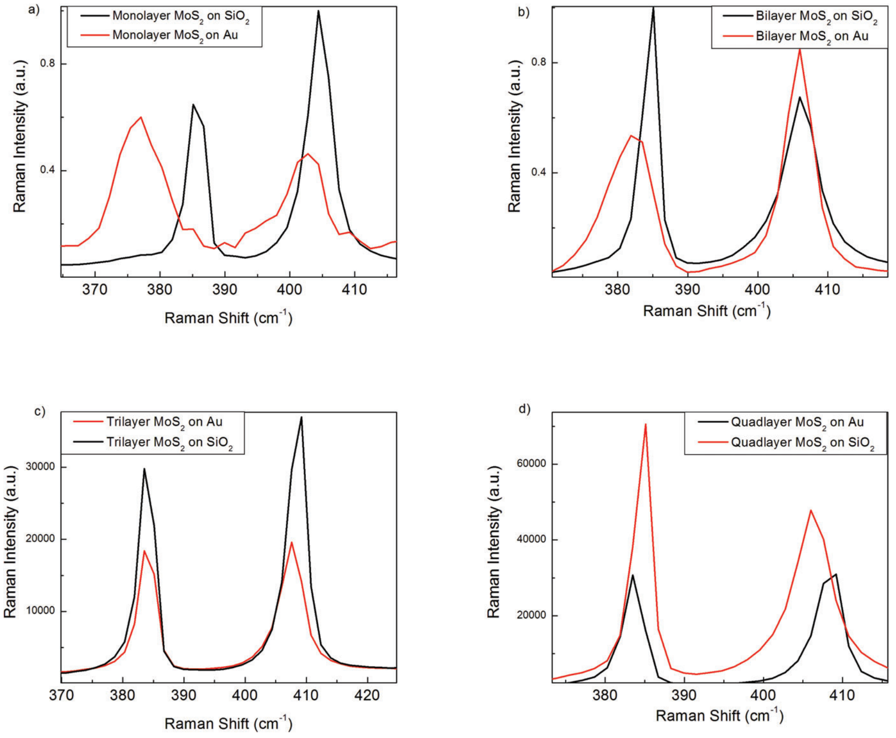

Figure 5.6: (a) The figure shows the Raman spectroscopy of a monolayer MoS2/SiO2 sample and a monolayer MoS2/Au sample measured at room temperature. We see a strong redshift of the Raman signature for MoS2/Au sample. (b) Graph showing the peak shift of bilayer MoS_2 from Au to SiO_2 (c) Graph showing the peak shift of trilayer MoS_2 from Au to SiO_2, (d) Graph showing the peak shift of quadlayer MoS_2 from Au to SiO_2. All data was acquired at room temperature.

5.2 Temperature Dependant Raman Spectroscopy

For the temperature dependant Raman spectroscopy data, the peaks shift from higher wavenumber to lower wavenumber as temperature goes up [28]. Previous studies of MoS_2 temperature dependence have found that as temperature goes up, there is a corresponding redshift in MoS_2's vibrational modes. We also expect a redshift and increase in intensity as layer number increases. As for the expected effects of different substrates, we expect MoS_2 to react differently depending if it is on a conductor, semiconductor, or insulator.

5.2.1 MoS_2/h-BN

For temperature dependant Raman measurements of MoS_2/h-BN, the 532 nm laser was set to a power of 5.28 mW. For monolayer MoS_2/h-BN, we observed that as temperature increased, both the E' peak and the A_1 peak redshifted. Additionally, as temperature goes up, there is an increase in intensity for both peaks as well as an increase in the width of both peaks. In figure 5.7, the E' peak was observed to occur around 375 cm^{-1} at 1.5k and 370 cm^{-1} for 300k. The A_1 peak was observed to occur around 395 cm^{-1} at 1.5k and 390 cm^{-1} at 300k. This is approximately a 5 cm^{-1} temperature induced redshift for both peaks. The intensity for the E' peak was about 870 arbitrary units (a.u.) at 1.5k and 950 a.u. at 300k corresponding to an increase of about 80 a.u. Similarly, the intensity for the A_1 peak was about 875 a.u. at 1.5k and 1000 a.u. at 300k, corresponding to an increase of 125 a.u., approximately. This redshift in peak position and increase in intensity as temperature increases has also been seen for temperature dependant measurements of MoS_2/SiO_2 such as in figure 5.5.

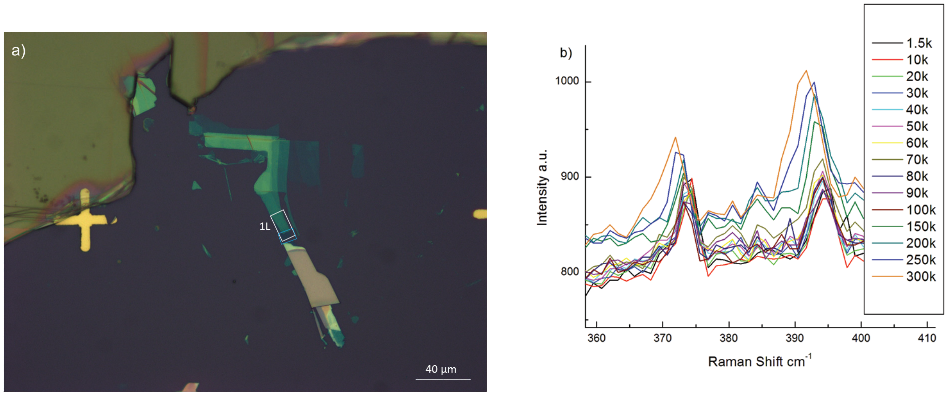

Figure 5.7: a) Picture of monolayer MoS_2 sample on h-BN at 50x magnification. SiO_2 is the substrate underneath the h-BN, and the crosses seen at the edges are way point markers used to help find the sample. The region the data was gathered from is boxed in white. The blue boxed region near the bottom of the white boxed region only rests on SiO_2, and this is where the data on SiO_2 was measured. b) The temperature dependant Raman spectroscopy data from monolayer MoS_2 on h-BN at temperatures ranging from 1.5k to 300k.

5.2.2 Monolayer MoS_2/Au

Raman spectroscopy was performed for monolayer MoS_2 on atomically flat Au, however, the signal to noise ratio was too low to obtain any meaningful data. Further, even when the laser was at a power of 5.28 mW (the highest power available in our system) and at exposure times exceeding 60 minutes, the monolayer signal was still too small even at temperatures above 1.5k as seen in figure 5.8. A second monolayer sample on atomically thin

Au was tested with the same system configurations (5.28 mW power, 532 nm laser, and 100x objective) and the signal to noise ratio was still too low. Again, we increased the exposure time to 60 minutes for the new monolayer sample and low signal to noise ratio still persisted. To verify that our system was working properly, we then took data from a nearby bilayer (again using 5.28 mW power, 532 nm laser, and 100x objective) and obtained signal from both the E' and A_1 peaks.

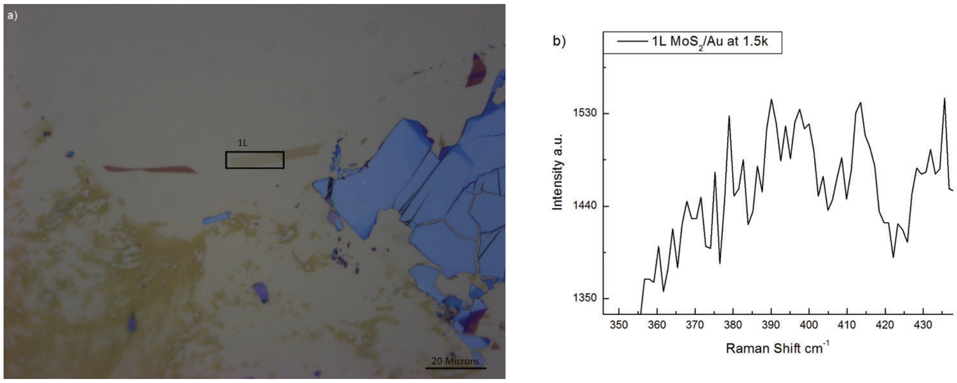

Figure 5.8: a) Picture of monolayer MoS_2 sample on atomically thin Au at 50x magnification. The region the data was gathered from is marked with a black box. b) The temperature dependant Raman data from monolayer MoS_2 on atomically thin Au at 1.5K.

5.2.3 Bilayer and Trilayer MoS_2/Au

For temperature dependant Raman measurements of 2L and 3L MoS_2/Au the laser was set to a power of 5.28 mW. For 2L and 3L MoS_2/Au, we observed that as temperature increased, both the E' peak and A_1 peak redshifted as seen in figures 5.9 and 5.10. Additionally, as temperature increased the widths and intensities of both peaks increased and this was similar for 2L and 3L MoS_2 samples. For both 2L and 3L MoS_2/Au the E' peak occurred at approximately 375 cm^{-1} at 1.5k and 370 cm^{-1} at 300k. Similarly, the A_1 peak for both 2L and 3L MoS_2/Au occurred at approximately 395 cm^{-1} at 1.5k and 390 cm^{-1} at 300k as seen in figures 5.9 and 5.10. This corresponds to approximately a 5 cm^{-1} redshift in both peaks on both layer numbers as temperature increased. In addition, for 2L - MoS_2/Au the intensities of the E' and A_1 peaks ranged from about 1000 a.u. to about 1300 a.u as seen in figure 5.9. For 3L - MoS_2/Au the intensities of both peaks ranged from about 1100 a.u. to about 1600 a.u as seen in figure 5.10. This increase in intensity as layer number increases is expected, but is not nearly as pronounced as it was for the Raman measurements at room temperature.

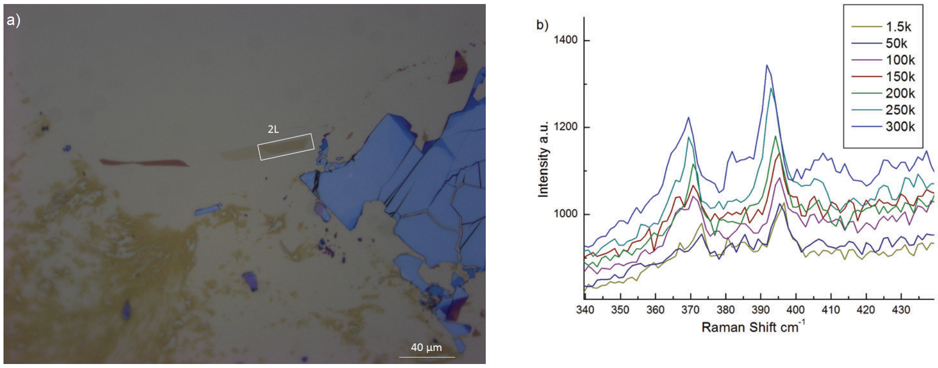

Figure 5.9: a) Picture of bilayer MoS_2 sample on atomically thin Au at 50x magnification. The region the data was gathered from is marked with a white box. b) The temperature dependant Raman data from bilayer MoS_2 on atomically thin Au at temperatures ranging from 1.5k to 300k.

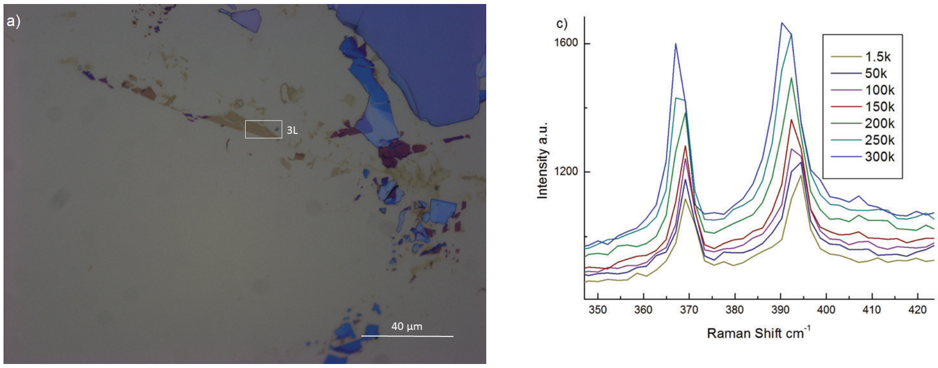

Figure 5.10: a) Picture of trilayer MoS_2 sample on atomically thin Au at 50x magnification. The region the data was gathered from is marked with a white box. b) The temperature dependant Raman data from trilayer MoS_2 on atomically thin Au at temperatures ranging from 1.5k to 300k.

In summary, we observe a redshift in both the E' and A_1 modes as temperature increases on all substrates. These results are similar for both 2L and 3L samples. The peaks shifting to lower wavenumber is expected since this behavior has been observed on SiO_2 and rough Au before [29].

5.2.4 Comparison of Bilayer and Trilayer Raman Spectroscopy data of MoS_2/Au

In the temperature dependence measurement for the bilayer and trilayer, for both the A_1 peak and E' peak, the positions of each peak shifted to lower wavenumber and intensities of each increased as temperature increased. Additionally, an increase in layer number causes the peaks to redshift and increase in intensity as seen in figure 5.11. The increase in intensity for the E' peak is about 100 a.u. and the increase in intensity for the A_1 peak is about 200 a.u. as seen in figure 5.11. For both 2L and 3L samples, the A_1 peak is more intense than the E' peak as seen in figures 5.9 and 5.10. These results on layer dependant peak position and intensity are similar to our findings for MoS_2/Au and MoS_2/SiO_2 at room temperature. Further study is needed to verify these results.

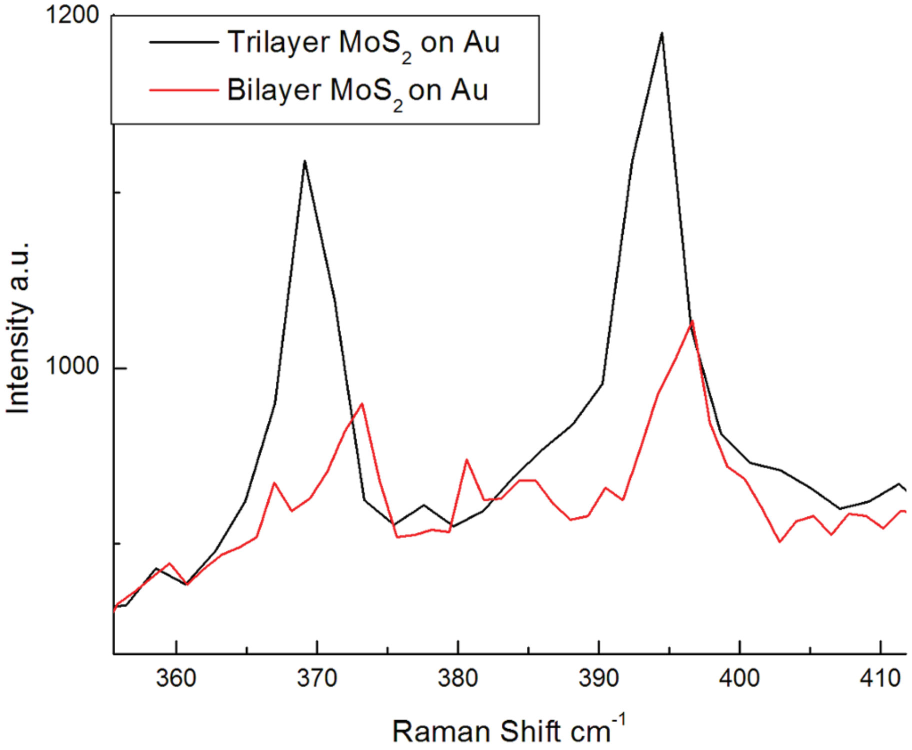

Figure 5.11: Plot of the raw raman data at 1.5k, with the trilayer plotted over the bilayer. One can clearly see the shift in peak position and change in intensity for both peaks from two layers to three layers.

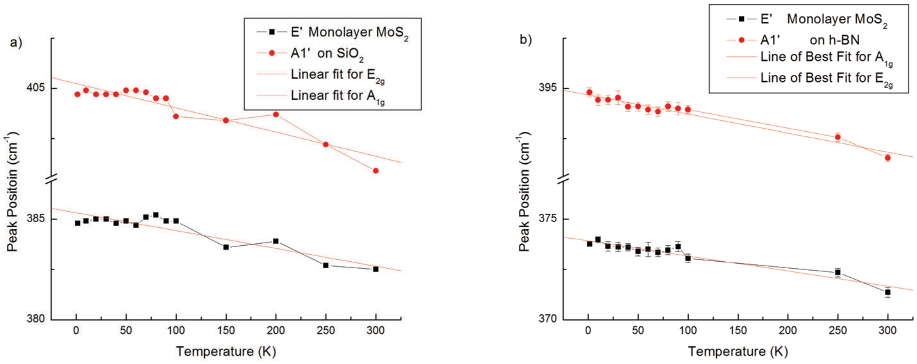

Figure 5.12: a) Peak positions vs temperature for monolayer MoS_2 on SiO_2 with applied linear fits. b) Peak positions vs temperature for monolayer MoS_2 on h-BN with applied linear fits. In both graphs, temperature is in kelvin and peak position is in cm^{-1}.

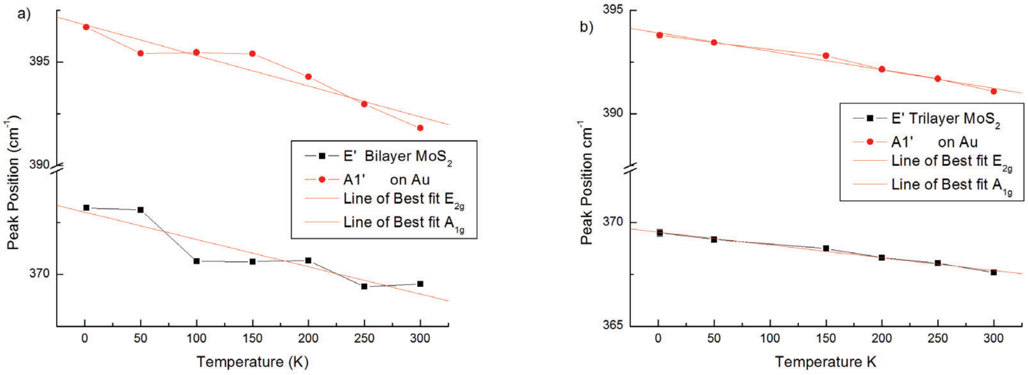

Figure 5.13: a) Peak positions vs temperature for bilayer MoS_2 on Au with applied linear fits. b) Peak positions vs temperature for trilayer MoS_2 on Au with applied linear fits. In both graphs, temperature is in kelvin and peak position is in cm^{-1}.

Alpha values are defined as $\omega = \omega_0 + \alpha T$ where ω_0 is the Raman peak at zero kelvin and α is the first order temperature coefficient. Alpha values are directly proportional to thermal conductivity and offer a useful way of seeing how this research compares to other sources from the literature. Alpha values attained for monolayer MoS_2/SiO_2 were at or slightly below literature values as shown in Table 1. The alpha values attained for monolayer MoS_2/h-BN were all consistently at or below literature values as shown in Table 2. For alpha values attained for bilayer MoS_2 on atomically thin Au, both E' and A_1 modes were above literature values as shown in Table 3. The alpha values attained for trilayer MoS_2 on atomically thin Au were mostly above literature values for both peaks as shown in Table 4.

1L	Temp. Range	Substrate	E' (cm^{-1}/K)	A_1 (cm^{-1}/K)
This Work	1.5 - 300 K	SiO_2	-0.008 +/- 0.001	-0.012 +/- 0.001
Sahoo et al. [28]	83 – 523 K	SiO_2	-0.013	-0.012
Yan et al. [30]	100 – 320 K	SiO_2		-0.013 +/- 0.001
Yan et al. [30]	100 – 320 K	SiO_2	-0.011 +/- 0.001	-0.013 +/- 0.001
Yan et al. [30]	100 – 320 K	SiO_2	–0.017	–0.013
Su et al. [31]	298.15 - 773.15 K	SiO_2	-0.024 ± 0.002	-0.062 ± 0.004
Su et al. [31]	298.15 - 773.15 K	SiO_2	–0.013	–0.016
Singh et al. [32]	100 – 300 K	SiO_2	–0.012	–0.014
Taube et al. [33]	70 - 350 K	SiO_2	–0.017	–0.013
Sarkar et al. [34]	8 K - 300 K	SiO_2	–0.015	–0.013
Sarkar et al. [34]	8 K - 300 K	SiO_2	0.013	0.013

Table 1: Alpha values for 1L - MoS_2/SiO_2. All values shown are in units of cm^{-1}/K. Values were derived from least squares fitting on the graphs of peak position vs temperature. Also note not every literature source had error values.

1L	Temp. Range	Substrate	E’ (cm^{-1}/K)	A_1 (cm^{-1}/K)
This Work	1.5 - 300 K	h-BN	-0.0076 +/- 0.001	-0.0091 +/- 0.001
Shen et al. [35]	78 K - 543 K	h-BN	−0.010	−0.014
Taube et al. [33]	70 - 350 K	h-BN	−0.012	−0.014
Yang et al. [36]	77 - 557 K	h-BN	-0.011	-0.009
Yang et al. [36]	77 - 557 K	h-BN	0.011	0.012

Table 2: Alpha values for 1L - MoS_2/h-BN. All values shown are in units of cm^{-1}/K. Values were derived from least squares fitting on the graphs of peak position vs temperature. Also note not every literature source had errors values.

2L	Temp. Range	Substrate	E’ (cm^{-1}/K)	A_1 (cm^{-1}/K)
This Work	1.5 - 300 K	Atomically Flat Au	-0.0135 +/- 0.0035	-0.0143 +/- 0.0052
Li et al. [37]	300 - 500 K	GaN	-0.018	−0.015
Bae et al. [29]	300 - 420 K	Rough Au	-0.011 +/- 0.0002	−0.012 +/- 0.0003
Zhang et al. [38]	300 - 500 K	Rough Au		-0.0139 ± 0.001
Majee et al. [39]	83 - 300 K	SiO_2	-0.009 +/- 0.003	−0.011 ± 0.005
Yu et al. [40]	300 - 500 K	Suspended		-0.020 +/- 0.001

Table 3: Alpha values for 2L - MoS_2/Au. All values shown are in units of cm^{-1}/K. Values were derived from least squares fitting on the graphs of peak position vs temperature. Also note not every literature source had errors values.

3L	Temp. Range	Substrate	E’ (cm^{-1}/K)	A_1 (cm^{-1}/K)
This Work	1.5 - 300 K	Atomically Flat Au	-0.0086 +/- 0.0027	-0.0115 +/- 0.0033
Lin et al. [41]	77 - 557 K	SiO_2	−0.006 +/- −0.001	−0.008 +/- −0.001
Sreeprasad et al. [42]	80 - 180 K	SiO_2	-0.027	-0.027
Yu et al. [43]	293.15 K	SiO_2	-0.026 +/- 0.001	

Table 4: Alpha values for 3L - MoS_2/Au. All values shown are in units of cm^{-1}/K. Values were derived from least squares fitting on the graphs of peak position vs temperature. Also note not every literature source had errors values.

One possible explanation for these results could be strain on the Mo - S bond by the Au substrate. Au has an electronegativity of 2.2 while Mo only has an electronegativity of 1.6. This could lead some S atoms to be more attracted to adjacent Au atoms rater than adjacent Mo atoms [44]. Another possible explanation could be doping from the Au substrate. As stated previously, since Au is more electronegative, p-doping might occur due to Au taking electrons from the valence band of MoS_2 and thus creating holes [45]. It has been shown before that intentional doping of MoS_2 with Au can induce similar shifts in the E' and A_1 Raman peaks [45]. It stands to reason that if doping did occur in one of the bilayer or trilayer samples, the resulting peak shift would look similar to what was seen in the data we gathered. [45] However, in either of the above cases, only the bottom-most layer in each of the samples was in contact with the substrate. Hence, the Raman signal from the bilayer and trilayer samples would largely resemble that of monolayer MoS_2.

5.3 Magnetic Field Dependant Raman Spectroscopy

For the magnetic field (B field) dependant Raman spectroscopy data, in our data we expect symmetry about 0 T and for the trend for + T to be mirrored for - T. B field dependence of MoS_2 on SiO_2 has been studied extensively, however, less is known about the B field dependence of the E' and A_1 modes on Au. For studies on monolayer MoS_2 on SiO_2 at room temperature with a perpendicular external B field, the A_1 mode has been shown to increase in intensity. However, the E' mode has been shown not to increase in intensity [46]. Since, A_1 is the out of plane vibrational mode of the S atoms and the E' mode is the in plane vibrational mode, this seems to suggest that the an externally applied perpendicular B field enhances the out of plane vibration of the S atoms in the lattice. Also in figure 5.14, one can see a very slight peak shift in both modes when going from 0T to 9T.

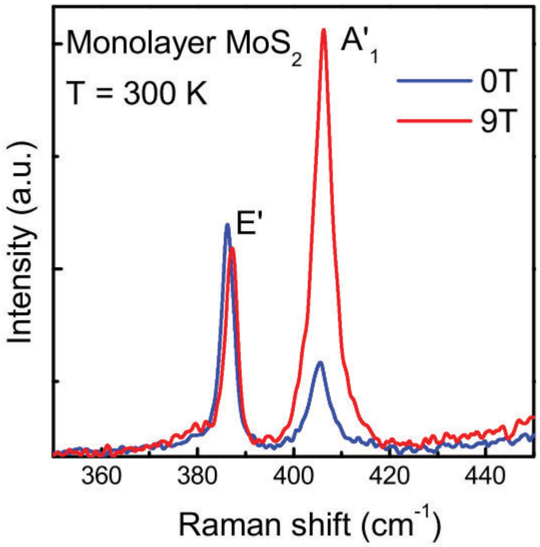

Figure 5.14: Magneto-Raman spectroscopy data for monolayer MoS$_2$ at 300k. This figure shows a drastic increase in the A_1 mode whereas the E' mode is relatively unchanged. Figure reproduced from Ji et al [46]

In the B field Raman spectroscopy measurement for the monolayer and bilayer on atomically thin Au, the observed correlation between peak position and B field was found to be negligible. To reiterate, all of these measurements were taken at 1.5k and all with the same specifications (5.28 mW power, 532 nm laser, and 100x magnification). We observe the intensities of both peaks increase as the intensity of the B field increases, but not nearly as much as what was seen in the literature. Further study is need to verify this lack of correlation.

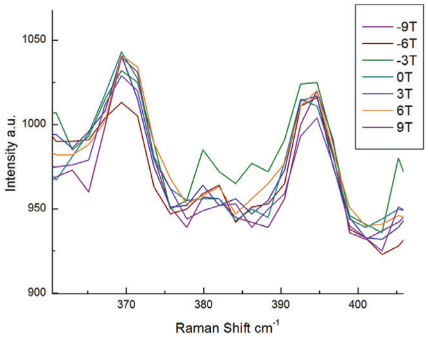

Figure 5.15: External B field dependant Raman data for MoS_2 on atomically thin Au. All measurements were performed at 1.5k. The range of magnetic field intensities goes from -9T to 9T.

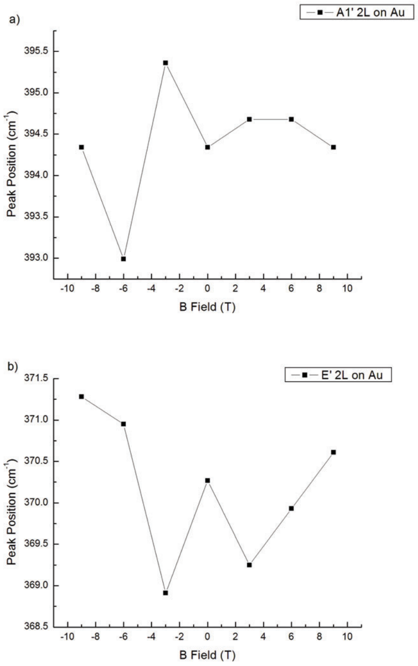

Figure 5.16: a) Peak positions vs B field for the A_1 peak on bilayer MoS_2 on Au. b) Peak positions vs B field for the E' peak on bilayer MoS_2 on Au. In both graphs, B field is in Tesla and peak position is in cm^{-1}.

6 Conclusion

In summary, the substrate dependant vibrational properties of MoS_2 were analyzed at different temperatures ranging from 1.5 K to 300 K and at magnetic field intensities ranging from -9T to 9T for mono, bi, tri, and quadlayer samples. The substrates tested were atomically flat Au, SiO_2, and h-BN. Low temperature Raman spectroscopy was measured using two system: (i) a homemade micro-Raman system equipped with a closed-cycle cryostat; and (ii) a commercial system- Renishaw Invia model. The closed-cycle cryostat, micro-raman system had a 532 nm laser and an objective of 100x magnification and the Renishaw Invia commercial Raman system used a 488 nm laser and a 50x objective of 0.85 numerical aperture. Once the data was collected, it was compiled and analyzed using Origin7 data analysis software. From this data, width, peak position, and intensity were plotted against temperature and magnetic field strength for each layer number. In the graphs of peak position vs. temperature, we observed an increase in intensity and redshift when layer number was increased. The peaks redshifted as temperature increased as well. Both the A1' and E' peaks were redshifted on atomically flat Au compared to their position in MoS_2/SiO_2. The graphs of peak position vs. temperature were fitted using a least squares linear regression and from this fit, the rates of change of Raman peak shift with respect to temperature (alpha values) were obtained. The α values for bilayer MoS_2 samples on atomically flat Au were found to be larger than all but 2 quoted literature values and α values for trilayer samples on Au were found to be smaller than all but one quoted literature value. Possible explanations for these results include strain on the Mo - S bonds by the Au substrate and doping by the Au substrate. However, further studies of temperature dependence and other parameters on atomically thin Au are needed to determine why this discrepancy arises.

7 Citations

References

[1] K. Novoselov, A. Geim, S. Morozov, Da Jiang, Yanshui Zhang, S. Dubonos, Irina Grigorieva, and A. Firsov. Electric field effect in atomically thin carbon films. *Nat. Mater.*, 6, 01 2004.

[2] Kaiying Dou, Yandong Ma, Rui Peng, and Wenhui Du. Promising valleytronic materials with strong spin-valley coupling in two-dimensional mn2x2 (m = mo, w; x = f, h). *Applied Physics Letters*, 117(17):172405, 2020.

[3] Md Rubayat-E Tanjil, Yunjo Jeong, Zhewen Yin, and Wyatt Panaccione. Ångström-scale, atomically thin 2d materials for corrosion mitigation and passivation. *Coatings*, 9(2), 2019.

[4] Graphene: Sheets of carbon-based nanoparticles. `https://www.dummies.com/education/science/nanotechnology/graphene-sheets-of-carbon-based-nanoparticles/`. Accessed: 2021-09-10.

[5] Queens university fl-graphene tem photo. `https://www.graphene-info.com/image-galleries/graphene-flakes-images`. Accessed: 2021-09-10.

[6] H. P. Boehm, A. Clauss, G. O. Fischer, and U. Hofmann. Das adsorptionsverhalten sehr dünner kohlenstoff-folien. *Zeitschrift für anorganische und allgemeine Chemie*, 316(3-4):119–127.

[7] F. Memarian, A. Fereidoon, and M. Darvish Ganji. Graphene young's modulus: Molecular mechanics and dft treatments. *Superlattices and Microstructures*, 85:348–356, 2015.

[8] Ali Eftekhari. Molybdenum diselenide (mose2) for energy storage, catalysis, and optoelectronics. *Applied Materials Today*, 8:1–17, 2017. 2D Materials in Electrochemistry.

[9] Najwa binti Hamzan, Calvin Yi Bin Ng, Rad Sadri, Min Kai Lee, and Lieh-Jeng Chang. Controlled physical properties and growth mechanism of manganese silicide nanorods. *Journal of Alloys and Compounds*, 851:156693, 2021.

[10] Ting Cao, Gang Wang, Wenpeng Han, H. Ye, Chuanrui Zhu, Junren Shi, and Qian Niu. Valley-selective circular dichroism of monolayer molybdenum disulphide. *Nature communications*, 3:887, 06 2012.

[11] Spi supplies molybdenum disulfide (mos2) crystal. `https://www.2spi.com/item/z429ml/molybdenum-disulfide-substrates/`. Accessed: 2021-09-10.

[12] Molybdenum disulfide (mos2) crystals. `https://graphene-supermarket.com/MoS2-Crystal.html`. Accessed: 2021-21-10.

[13] Ming-hong Wu, Lin Li, Ning Liu, De-jin Wang, and Yuan-cheng Xue. Molybdenum disulfide (mos 2) as a co-catalyst for photocatalytic degradation of organic contaminants: A review. *Process Safety and Environmental Protection*, 118, 06 2018.

[14] Exciton. `https://en.wikipedia.org/wiki/Exciton#text=An20exciton20is20a20bound,insulators2C20semiconductors20and20some20liquids`. Accessed: 2021-09-10.

[15] Katsuyoshi Kobayashi and Jun Yamauchi. Electronic structure and scanning-tunneling-microscopy image of molybdenum dichalcogenide surfaces. *Phys. Rev. B*, 51:17085–17095, Jun 1995.

[16] Ferdows Zahid, Lei Liu, Yu Zhu, and Wang. A generic tight-binding model for monolayer, bilayer and bulk mos2. *AIP Advances*, 3(5):052111, 2013.

[17] Sefaattin Tongay, Sima S. Varnoosfaderani, Bill R. Appleton, and Junqiao Wu. Magnetic properties of mos2: Existence of ferromagnetism. *Applied Physics Letters*, 101(12):123105, 2012.

[18] Hexagonal boron nitride (h-bn). `https://www.2dsemiconductors.com/hexagonal-boron-nitride-h-bn/`. Accessed: 2021-09-10.

[19] Hexagonal boron nitride (h-bn) crystals and films. `https://www.ossila.com/products/hexagonal-boron-nitride`. Accessed: 2021-09-10.

[20] February 1928: Raman scattering discovered. `http://www.aps.org/publications/apsnews/200902/physicshistory.cfm`.

[21] Lesson 1. basic of raman scattering. `https://www.nanophoton.net/lecture-room/raman-spectroscopy/lesson-1-1`. Accessed: 2021-09-10.

[22] File:raman energy levels.jpg. `https://commons.wikimedia.org/wiki/File:Raman_energy_levels.jpg`. Accessed: 2021-09-10.

[23] The raman spectrophotometer. `https://www.sas.upenn.edu/~crulli/TheRamanSpectrophotometer.html`. Accessed: 2021-09-10.

[24] J. Ribeiro-Soares, R. M. Almeida, E. B. Barros, P. T. Araujo, and M. S. Dresselhaus. Group theory analysis of phonons in two-dimensional transition metal dichalcogenides. *Phys. Rev. B*, 90:115438, Sep 2014.

[25] Katarzyna Golasa, Maciej Molas, K. Nogajewski, and Magdalena Grzeszczyk. The effect of substrate on vibrational properties of single-layer mos$_2. Acta Physica Polonica A, 130 : 1172 - -1175, 112016.$

[26] Jian Yuan, Meng Zhao, Wengzhi Yu, Yao Lu, Caiyun Chen, Meng Xu, Shaojuan Li, Kian Ping Loh, and Bao Qiaoliang. Raman spectroscopy of two-dimensional bi2texse3 x platelets produced by solvothermal method. *Materials*, 8(8):5007–5017, 2015.

[27] Prachi Budania, Paul T. Baine, John H. Montgomery, David W. McNeill, S.J. Neil Mitchell, Mircea Modreanu, and Paul K. Hurley. Comparison between scotch tape and gel-assisted mechanical exfoliation techniques for preparation of 2d transition metal dichalcogenide flakes. *Micro & Nano Letters*, 12(12):970–973, 2017.

[28] Satyaprakash Sahoo, Anand P. S. Gaur, Majid Ahmadi, Maxime J.-F. Guinel, and Ram S. Katiyar. Temperature-dependent raman studies and thermal conductivity of few-layer mos2. *The Journal of Physical Chemistry C*, 117(17):9042–9047, 2013.

[29] Jung Jun Bae, Hye Yun Jeong, Gang Hee Han, Jaesu Kim, Hyun Kim, Min Su Kim, Byoung Hee Moon, Seong Chu Lim, and Young Hee Lee. Thickness-dependent in-plane thermal conductivity of suspended mos2 grown by chemical vapor deposition. *Nanoscale*, 9:2541–2547, 2017.

[30] Rusen yan, Jeffrey R. Simpson, Simone Bertolazzi, Jacopo Brivio, Michael Watson, Xufei Wu, Andras Kis, Tengfei Luo, Angela R. Hight Walker, and Huili Grace Xing. Thermal conductivity of monolayer molybdenum disulfide obtained from temperature-dependent raman spectroscopy. *ACS Nano*, 8(1):986–993, 2014. PMID: 24377295.

[31] Liqin Su, Yong Zhang, Yifei Yu, and Linyou Cao. Dependence of coupling of quasi 2-d mos2 with substrates on substrate types, probed by temperature dependent raman scattering. *Nanoscale*, 6(9):4920–4927, 2014.

[32] Manavendra P. Singh, Manab Mandal, K. Sethupathi, M. S. Ramachandra Rao, and Pramoda K. Nayak. Study of thermometry in two-dimensional sb2te3 from temperature-dependent raman spectroscopy. *Nanoscale Research Letters*, 16(1), 2021.

[33] Andrzej Taube, Jarosław Judek, Anna Łapińska, and Mariusz Zdrojek. Temperature-dependent thermal properties of supported mos2 monolayers. *ACS Applied Materials & Interfaces*, 7(9):5061–5065, 2015. PMID: 25706435.

[34] Suman Sarkar, Indrajit Maity, H. L. Pradeepa, Goutham Nayak, Laetitia Marty, Julien Renard, Johann Coraux, Nedjma Bendiab, Vincent Bouchiat, Sarthak Das, and et al. Anharmonicity in raman-active phonon modes in atomically thin mos2. *Physical Review B*, 101(20), 2020.

[35] Pengfei Shen, Xigui Yang, Mingrun Du, and Huafang Zhang. Temperature and laser-power dependent raman spectra of mos2/rgo hybrid and few-layered mos2. *Physica B: Condensed Matter*, 604:412693, 2021.

[36] Mei Yang, Xuerui Cheng, Yuanyuan Li, Yufen Ren, Miao Liu, and Zeming Qi. Anharmonicity of monolayer mos2, mose2, and wse2: A raman study under high pressure and elevated temperature. *Applied Physics Letters*, 110(9):093108, 2017.

[37] Zhiwen Li, Jiangliu Luo, Shengqun Hu, Qiang Liu, Wenjie Yu, Youming Lu, and Xinke Liu. Strain enhancement for a mos2-on-gan photodetector with an al2o3 stress liner grown by atomic layer deposition. *Photon. Res.*, 8(6):799–805, Jun 2020.

[38] Xian Zhang, Dezheng Sun, Yilei Li, Gwan-Hyoung Lee, Xu Cui, Daniel Chenet, Yumeng You, Tony F. Heinz, and James C. Hone. Measurement of lateral and interfacial thermal conductivity of single- and bilayer mos2 and mose2 using refined optothermal raman technique. *ACS Applied Materials & Interfaces*, 7(46):25923–25929, 2015. PMID: 26517143.

[39] Bishnu Pada Majee, Jay Deep Gupta, Abhishek Sanskrityayn, and Ashish Kumar Mishra. Thermal sensitive quantum and phonon confinement in semiconducting triangular-shaped mos2. *The Journal of Physical Chemistry C*, 125(27):14865–14873, 2021.

[40] Yifei Yu, Tamzid Minhaj, Lujun Huang, Yiling Yu, and Linyou Cao. In-plane and interfacial thermal conduction of two-dimensional transition-metal dichalcogenides. *Phys. Rev. Applied*, 13:034059, Mar 2020.

[41] Zhongtao Lin, Wuguo Liu, Shibing Tian, Ke Zhu, Yuan Huang, and Yang Yang. Thermal expansion coefficient of few-layer mos2 studied by temperature-dependent raman spectroscopy. *Scientific Reports*, 11(1), 2021.

[42] T. S. Sreeprasad, Phong Nguyen, Namhoon Kim, and Vikas Berry. Controlled, defect-guided, metal-nanoparticle incorporation onto mos2 via chem-

ical and microwave routes: Electrical, thermal, and structural properties. *Nano Letters*, 13(9):4434–4441, 2013. PMID: 23927716.

[43] Yifei Yu, Tamzid Minhaj, Lujun Huang, Yiling Yu, and Linyou Cao. In-plane and interfacial thermal conduction of two-dimensional transition-metal dichalcogenides. *Physical Review Applied*, 13(3), 2020.

[44] Erik Pollmann, Stephan Sleziona, Tobias Foller, Ulrich Hagemann, Claudia Gorynski, Oliver Petri, Lukas Madauss, Lars Breuer, and Marika Schleberger. Large-area, two-dimensional mos2 exfoliated on gold: Direct experimental access to the metal–semiconductor interface. *ACS Omega*, 6(24):15929–15939, 2021.

[45] Matej Velicky, Alvaro Rodriguez, Milan Bousa, Andrey V. Krayev, Martin Vondracek, Jan Honolka, Mahdi Ahmadi, Gavin E. Donnelly, Fumin Huang, Hector D. Abruna, Kostya S. Novoselov, and Otakar Frank. Strain and charge doping fingerprints of the strong interaction between monolayer mos2 and gold. *The Journal of Physical Chemistry Letters*, 11(15):6112–6118, 2020. PMID: 32633525.

[46] Jianting Ji, Anmin Zhang, Jiahe Fan, Yuesheng Li, Xiaoqun Wang, Jiandi Zhang, E. W. Plummer, and Qingming Zhang. Giant magneto-optical raman effect in a layered transition metal compound. *Proceedings of the National Academy of Sciences*, 113(9):2349–2353, 2016.

99